Onset of triaxial deformation in ^{66}Zn and properties of its first excited 0^+ state studied by means of Coulomb excitation

M. Rocchini,[1,2,3,*] K. Hadyńska-Klęk,[4,5] A. Nannini,[1,2] A. Goasduff,[6,7] M. Zielińska,[8] D. Testov,[6,7] T. R. Rodríguez,[9] A. Gargano,[10] F. Nowacki,[11] G. De Gregorio,[10,12] H. Naïdja,[13] P. Sona,[1,2] J. J. Valiente-Dobón,[4] D. Mengoni,[6,7] P. R. John,[6,7,14] D. Bazzacco,[6,7] G. Benzoni,[15] A. Boso,[6,7] P. Cocconi,[4] M. Chiari,[1,2] D. T. Doherty,[16] F. Galtarossa,[4] G. Jaworski,[4] M. Komorowska,[5] N. Marchini,[1,17] M. Matejska-Minda,[5,18] B. Melon,[1] R. Menegazzo,[6,7] P. J. Napiorkowski,[5] D. Napoli,[4] M. Ottanelli,[1] A. Perego,[1,2] L. Ramina,[7] M. Rampazzo,[7] F. Recchia,[6,7] S. Riccetto,[19,20] D. Rosso,[4] and M. Siciliano[4,6]

[1]*INFN Sezione di Firenze, IT-50019 Firenze, Italy*
[2]*Università degli Studi di Firenze, Dipartimento di Fisica e Astronomia, IT-50019 Firenze, Italy*
[3]*Department of Physics, University of Guelph, N1G2W1 Guelph, Canada*
[4]*INFN Laboratori Nazionali di Legnaro, IT-35020 Padova, Italy*
[5]*Heavy Ion Laboratory, University of Warsaw, PL-02-093 Warszawa, Poland*
[6]*Università degli Studi di Padova, Dipartimento di Fisica e Astronomia, IT-35131 Padova, Italy*
[7]*INFN Sezione di Padova, IT-35131 Padova, Italy*
[8]*IRFU, CEA, Université Paris-Saclay, F-91191 Gif-sur-Yvette, France*
[9]*Departamento de Física Teórica and CIAFF, Universidad Autónoma de Madrid, E-28049 Madrid, Spain*
[10]*INFN Sezione di Napoli, IT-80126 Napoli, Italy*
[11]*Université de Strasbourg, IPHC/CNRS, F-67037 Strasbourg, France*
[12]*Dipartimento di Matematica e Fisica, Università degli Studi della Campania "Luigi Vanvitelli", I-81100 Caserta, Italy*
[13]*LPMS, Université Constantine 1, Route Ain-El bey, 25000 Constantine, Algérie*
[14]*Institut für Kernphysik, Technische Universität Darmstadt, D-64289 Darmstadt, Germany*
[15]*INFN Sezione di Milano, IT-20133 Milano, Italy*
[16]*Department of Physics, University of Surrey, GU2 7XH Guildford, United Kingdom*
[17]*Università degli Studi di Camerino, Dipartimento di Fisica, IT-62032 Camerino, Italy*
[18]*Institute of Nuclear Physics, Polish Academy of Sciences, PL-31342 Kraków, Poland*
[19]*Università degli Studi di Perugia, Dipartimento di Fisica e Geologia, IT-06123 Perugia, Italy*
[20]*INFN Sezione di Perugia, IT-06123 Perugia, Italy*

(Received 19 August 2020; accepted 18 December 2020; published 19 January 2021)

The electromagnetic structure of ^{66}Zn at low excitation energy was investigated via low-energy Coulomb excitation at INFN Legnaro National Laboratories, using the Gamma Array of Legnaro Infn Laboratories for nuclEar spectrOscopy (GALILEO) γ-ray spectrometer coupled to the SPIDER (Silicon PIe DEtectoR). A set of reduced $E2$, $E3$, and $M1$ matrix elements was extracted from the collected data using the GOSIA code, yielding 12 reduced transition probabilities between the low-spin states and the spectroscopic quadrupole moment of the 2_1^+ state. The $B(E2)$ values for transitions depopulating the 0_2^+ state have been determined for the first time, allowing for the lifetime of this state to be deduced and, consequently, the $\rho^2(E0; 0_2^+ \rightarrow 0_1^+)$ monopole transition strength to be extracted. In addition, the $B(E3; 3_1^- \rightarrow 0_1^+)$ value has been determined for the first time in a Coulomb excitation experiment. The obtained results resolve the existing discrepancies between literature lifetimes and demonstrate that ^{66}Zn cannot be described by using simple collective models. Therefore, new state-of-the-art beyond-mean-field and large-scale shell-model calculations were performed in order to interpret the structure of this nucleus. Both the experimental and theoretical results suggest that the triaxial degree of freedom has an important impact on electromagnetic properties of ^{66}Zn, while the unique features of the 0_2^+ state indicate its distinct and rather isolated structure.

DOI: 10.1103/PhysRevC.103.014311

I. INTRODUCTION

The collective properties of stable zinc isotopes have been in focus of detailed experimental and theoretical studies for the past decades. Being located only two protons above the magic Ni nuclei ($Z = 28$) and close to the neutron mid-shell between $N = 28$ and $N = 50$, these nuclei provide ideal opportunities to study the interplay of microscopic and macroscopic degrees of freedom in nuclear matter, particularly with respect to shape coexistence and shape transition phenomena. The former has been established in the neighboring Se, Ge, and Ni isotopes [1–5], while no clear evidence has yet been

*mrocchin@uoguelph.ca

 ©2021 American Physical Society

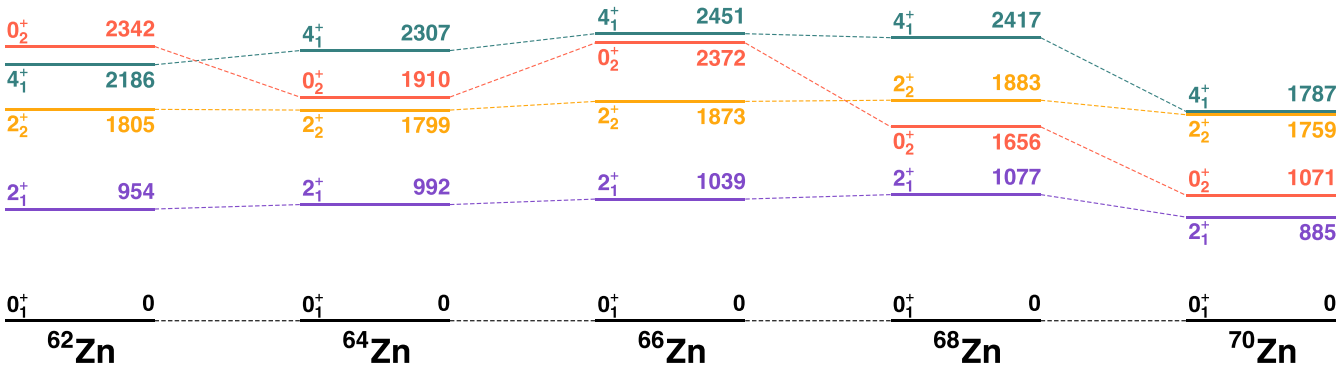

FIG. 1. Energy systematics of low-lying states in Zn isotopes with $N = 32$–40. All energies are given in keV.

reported in the Zn isotopic chain. The only exception is ^{68}Zn, where the $0_2{}^+$ state has been suggested to be the bandhead of a more deformed structure than that built on the ground state [6]. A shape transition from the almost spherical nuclei near ^{70}Zn ($N = 40$ subshell closure) to the γ-soft lighter Zn isotopes has also been predicted [7,8], although firm experimental evidence supporting this scenario is still missing.

Traditionally, the structure of even-even stable Zn isotopes was ascribed to the vibrational motion [9,10], mainly on the basis of the energy pattern of the first few excited states. The presence of possible two-phonon triplets ($0_2{}^+$, $2_2{}^+$, $4_1{}^+$ states) at about twice the energy of the first excited $2_1{}^+$ states (Fig. 1) seems to support such picture. However, while the energies of the $2_1{}^+$, $2_2{}^+$, and $4_1{}^+$ states evolve slowly and smoothly as a function of the neutron number, the $0_2{}^+$ state follows a different pattern, with a much more rapid decrease of its excitation energy from ^{62}Zn to ^{70}Zn, interrupted by a sudden jump observed for ^{66}Zn. The vibrational interpretation definitely fails when other electromagnetic properties are taken into account, such as transition probabilities and quadrupole moments, similar to what was found for instance in the Cd isotopes [11,12]. Quasirotational $K = 0$ and $K = 2$ bands were suggested in ^{64}Zn and ^{66}Zn, based on the enhanced in-band transitions (i.e., $6_1{}^+ \rightarrow 4_1{}^+ \rightarrow 2_1{}^+$ and $6_2{}^+ \rightarrow 4_2{}^+ \rightarrow 2_2{}^+$) and weak intraband transitions [13,14]. In addition, the $B(E2)$ and $B(M1)$ values from 2^+ and 1^+ states in ^{66}Zn agree reasonably well with the γ-soft interpretation [15].

Notably, all the main paradigms of collective nuclear excitations have been considered to describe the structure of the stable Zn isotopes over the past decades, particularly in the case of ^{66}Zn. One of the reasons why multiple interpretations seem to fit the experimental data equally well is related to the contradictions present in the literature regarding some key observables in ^{66}Zn, such as the $B(E2; 4_1{}^+ \rightarrow 2_1{}^+)$, $B(E2; 2_2{}^+ \rightarrow 2_1{}^+)$, and $Q_s(2_1{}^+)$ values. In addition, for transitions de-exciting the $0_2{}^+$ state, only upper limits of the $E2$ transition strengths are known, while no decays from higher lying 2^+ states to the $0_2{}^+$ state have been identified.

In order to investigate the collective properties of ^{66}Zn at low excitation energy, a dedicated low-energy multistep Coulomb-excitation experiment was performed. This experimental technique is ideally suited to determine reduced transition probabilities between low-lying states as well as their spectroscopic quadrupole moments, which can be extracted in a model-independent way. Furthermore, thanks to the unique information on relative signs of matrix elements, which can be obtained solely with multistep Coulomb excitation, it is possible to apply the quadrupole sum rule method to determine the quadrupole deformation of the nucleus in its individual states [16]. In view of the experimental results, the electromagnetic properties of ^{66}Zn have been interpreted in the framework of state-of-the-art microscopic calculations within the beyond-mean-field theory and various large-scale shell-model approaches, with a particular focus on the collective properties of the observed states.

This paper is organized as follows: The experimental details are presented in Sec. II, while the Coulomb-excitation data analysis and the experimental results are described in Sec. III. In Sec. IV, those results are discussed in the context of the quadrupole sum rules analysis (Sec. IV A), beyond-mean-field theory (Sec. IV B), and large-scale shell models (Sec. IV C).

II. EXPERIMENTAL DETAILS

A dedicated experiment to study the structure of ^{66}Zn at low excitation energy was performed at the INFN Legnaro National Laboratories (LNL) in Italy [17]. A continuous ^{66}Zn beam of 240-MeV energy was delivered by the XTU-Tandem accelerator and impinged on an enriched ^{208}Pb target. The beam energy was chosen to be as high as possible while still fulfilling the Cline's safe distance criterion [18], which ensures a purely electromagnetic interaction between the collision partners if their surfaces are separated by at least 5 fm. The energy used in the present experiment corresponded to the distance of 7 fm between the nuclear surfaces in head-on collisions. Thanks to the use of a heavy target, the probability of multistep excitation and reorientation effects was enhanced, increasing the experimental sensitivity to spectroscopic quadrupole moments and relative signs of transitional matrix elements [19]. Additionally, the choice of ^{208}Pb as a target material ensured that there was no overlap of γ rays resulting from target excitation with transitions in ^{66}Zn. The Gamma Array of Legnaro Infn Laboratories for nuclEar spectrOscopy (GALILEO) spectrometer [20,21] was used to detect γ rays depopulating the Coulomb-excited states, while the scattered ^{66}Zn nuclei were detected in the Silicon PIe

DEtectoR (SPIDER) array [22], used for the first time in the present experiment. Signals coming from both detector arrays were collected and processed using a fully digital acquisition system, operating in a self-trigger mode [21]. Single γ-ray and particle spectra were acquired, while the final γ-particle coincidences were reconstructed in the offline analysis. The dead time for each channel was kept below 1% throughout the experiment. In total, data were collected during ≈68 h with an average beam intensity of 1.3 pnA.

During the experiment, the GALILEO spectrometer consisted of 24 HPGe detectors arranged in four rings: 4 detectors were placed at 152°, 5 at 129°, 5 at 119°, and the remaining 10 detectors at 90° (all angles given relative to the beam direction). Each HPGe detector was enclosed in a BGO anti-Compton shield. A 22-cm-diameter vacuum chamber hosting the target and the SPIDER array was positioned in the center of the GALILEO spectrometer, resulting in a 25(1)-cm distance between the target and the HPGe front surface. Lead collimators were placed in front of every GALILEO HPGe crystal to avoid the direct detection of γ rays by the BGO shields, limiting the active surface of each detector to 17.3 cm^2. The γ-ray energy and efficiency calibrations where performed up to 1.8 MeV energy, using the standard ^{22}Na, ^{54}Mn, ^{60}Co, ^{88}Y, ^{137}Ba, ^{137}Cs, and ^{152}Eu sources. For the full GALILEO array, an energy resolution of 0.2% and an absolute efficiency of 2.0% were measured at 1332.5 keV.

SPIDER is an array of independent silicon detectors, individually segmented on the front surface into eight annular strips. These detectors are characterized by an excellent energy resolution (about 1% for 5.5-MeV α particles, when coupled to the GALILEO array) and a segmentation sufficient to achieve about 1% resolution for γ-ray energy after applying Doppler-correction procedures in the present experimental conditions. The energy calibration of individual SPIDER segments was performed with a triple-α source (^{239}Pu + ^{241}Am + ^{244}Cm) and a pulse generator, and the measured calibration was extrapolated to the energy range of scattered particles (which reached ≈75 MeV in the present experiment). This SPIDER initial calibration was refined by minimizing the Doppler broadening of the measured $2_1^+ \rightarrow 0_1^+$ transition in ^{66}Zn. During the experiment the SPIDER array was positioned at backward angles with respect to the beam direction, in order to reduce radiation damage effects. Such a configuration also enhances the effect of spectroscopic quadrupole moments and relative signs of transitional matrix elements on the measured excitation cross sections. In the present experiment, a total of seven trapezoidal silicon detectors were arranged inside the scattering chamber in a cone-like configuration described in detail in Ref. [22]. The exact position of the SPIDER frame with respect to the beam direction was again found by minimizing the Doppler broadening of the $2_1^+ \rightarrow 0_1^+$ transition of ^{66}Zn, and the detector was found to be off center by less than 5 mm. The angular coverage in the present experiment was $123.5^{+1.2}_{-0.9}$ to $161.3^{+1.8}_{-1.3}$ deg, where the error bars reflect the off centering. In such geometry, the SPIDER array covers about 17% of 4π solid angle.

In the multistep Coulomb-excitation process, excited states in the nuclei of interest can be populated via various paths, involving different intermediate states. Consequently, the measured excitation cross sections may depend on multiple matrix elements in a complex nonlinear way. In order to disentangle their individual contributions, the subdivision of the experimental data with respect to the projectile scattering angle was performed. Eight different angular ranges could be selected thanks to the SPIDER segmentation: 123.5–127.5°, 127.5–131.8°, 131.8–136.4°, 136.4–141.2°, 141.2–146.1°, 146.1–151.2°, 151.2–156.3°, and 156.3–161.3°.

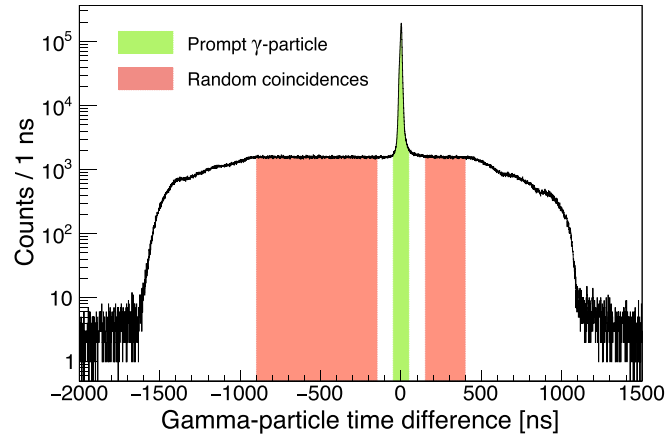

FIG. 2. γ-particle coincidence spectrum. The gate used to select the prompt coincidences is marked in green (light gray), while the two regions considered for the random-coincidence subtraction are marked in red (dark gray).

The target thickness was precisely determined from the online particle spectra acquired with the SPIDER array, resulting in $d = 0.616(11)$ mg/cm^2 [23]. A similar result [$d = 0.640(30)$ mg/cm^2] was obtained in an independent measurement performed at the INFN LABEC laboratory in Florence [24] using the Rutherford back-scattering technique. Furthermore, a built-up carbon layer was identified on the surface of the target, with a measured thickness of 0.114(12) mg/cm^2 [23]. The reduction of the projectile energy caused by this layer, equal to 4.3(5) MeV, was taken into account in the data analysis.

The Compton suppression and pile-up rejection procedures were applied for all individual GALILEO detectors during the online data acquisition process and then optimized in the offline analysis. Additionally, pile-up rejection was implemented for each SPIDER strip. The γ-particle coincidences were selected using three different software filters based on particle energy, event multiplicity, and γ-particle time coincidence. Since in the present experiment SPIDER was positioned at backward angles, and consequently only the scattered ^{66}Zn ions were detected, the particle-energy selection was used solely to eliminate the noise appearing in the low-energy region of the spectrum, which could be associated with random coincidences. Hence, only the events with multiplicity equal to 1 for the ^{66}Zn scattered projectiles were selected. A time interval of 100 ns for the γ-particle coincidence gate was required in the offline analysis and a random-coincidence subtraction was performed, as presented in Fig. 2.

Spectra collected in the individual HPGe detectors were summed up in the offline analysis process. Figure 3 shows the total GALILEO γ-ray spectrum in coincidence with back-

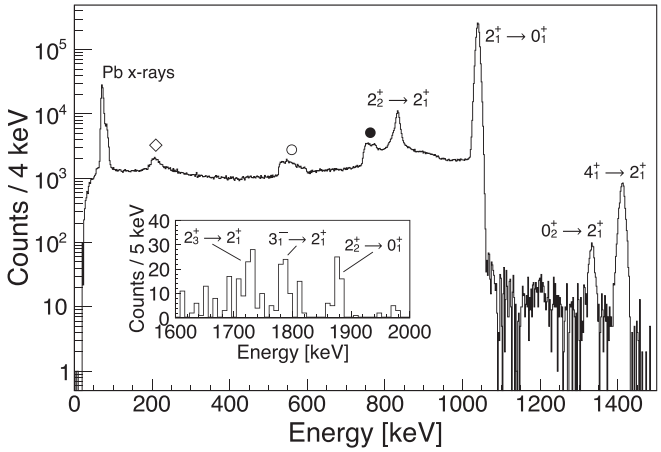

FIG. 3. Experimental spectrum of γ rays detected in the GALILEO spectrometer in coincidence with back-scattered ^{66}Zn ions detected in the SPIDER array, Doppler-corrected for the projectile velocity. Doppler-broadened transitions resulting from excitation of target contaminants are marked with circles (full for ^{206}Pb and open for ^{207}Pb). The structure marked with an open diamond results from Compton back-scattering of γ rays on materials surrounding the detectors. The inset shows the high-energy portion of the spectrum with three weak γ-ray transitions of ^{66}Zn.

scattered ^{66}Zn particles, after the Doppler correction for the velocity of the projectile nuclei. The velocity was determined event by event from the energy and position registered in SPIDER. After all optimization procedures applied to the collected data, an energy resolution of 1.1% was achieved for the 1039-keV $2_1^+ \rightarrow 0_1^+$ transition in ^{66}Zn.

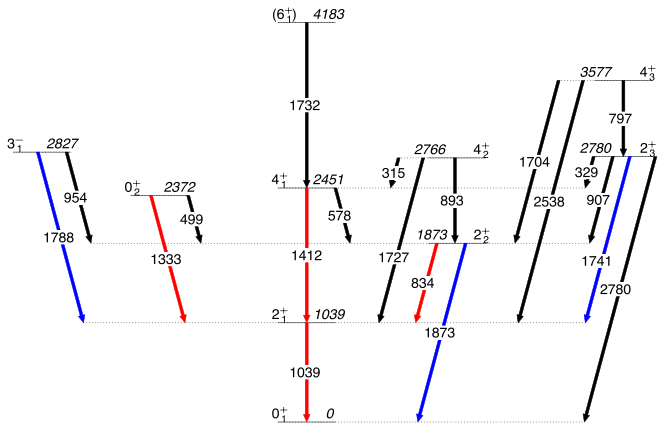

FIG. 4. Low-lying level scheme of the ^{66}Zn isotope relevant for the present work. The number of counts in the transitions marked in red (light gray) was sufficient to subdivide the data into eight angular ranges, exploiting the segmentation of the SPIDER detector to the fullest, while for the transitions marked in blue (dark gray) the total number of counts in coincidence with the SPIDER array was used in the analysis. Transitions marked in black have not been observed in the present experiment; however, the corresponding matrix elements were considered in the Coulomb-excitation data analysis with the GOSIA code. The hypothetical 2^+ state introduced in the GOSIA analysis as a buffer state for the 0_2^+ level (see the text for further details) is not shown.

TABLE I. Total numbers of counts in the observed γ-ray transitions and their relative efficiency-corrected intensities, normalized to that of the $2_1^+ \rightarrow 0_1^+$ transition.

Transition	Energy (keV)	Counts	Relative intensity
$2_1^+ \rightarrow 0_1^+$	1039	$1.49(4) \times 10^6$	1
$2_2^+ \rightarrow 2_1^+$	833	$3.7(4) \times 10^4$	$2.2(3) \times 10^{-2}$
$4_1^+ \rightarrow 2_1^+$	1412	$6.4(5) \times 10^3$	$5.1(5) \times 10^{-3}$
$0_2^+ \rightarrow 2_1^+$	1333	$6.8(13) \times 10^2$	$5.3(10) \times 10^{-4}$
$2_3^+ \rightarrow 2_1^+$	1741	75(30)	$7(3) \times 10^{-5}$
$3_1^- \rightarrow 2_1^+$	1787	66(20)	$6.0(19) \times 10^{-5}$
$2_2^+ \rightarrow 0_1^+$	1873	60(17)	$5.6(17) \times 10^{-5}$

The low-energy level scheme of ^{66}Zn relevant for the present data analysis is shown in Fig. 4. The observed γ-ray transitions are marked in red and blue and their intensities are reported in Table I. For the transitions marked in red (i.e., $2_1^+ \rightarrow 0_1^+$, $4_1^+ \rightarrow 2_1^+$, $2_2^+ \rightarrow 2_1^+$, and $0_2^+ \rightarrow 2_1^+$), the registered number of counts was sufficient to exploit the full segmentation of the SPIDER array, and thus to divide the data into eight angular ranges defined by the width of each strip. Furthermore, three weaker transitions were observed, namely $2_3^+ \rightarrow 2_1^+$, $3_1^- \rightarrow 2_1^+$, and $2_2^+ \rightarrow 0_1^+$ (marked in blue in Fig. 4, and presented in the inset of Fig. 3). As the numbers of counts in those transitions were insufficient to subdivide the data into angular ranges, they were analyzed in coincidence with the full detection range of the SPIDER array.

III. COULOMB-EXCITATION DATA ANALYSIS

A set of reduced electromagnetic matrix elements was extracted from the measured γ-ray yields using the GOSIA code [18,25], which performs a multidimensional χ^2 minimization constrained by complementary spectroscopic information, such as branching ratios, $E2/M1$ mixing ratios, and lifetimes measured in previous experiments.

The level scheme of ^{66}Zn considered in the current analysis (presented in Fig. 4) is known from previous experiments: Coulomb excitation, β^- decay of ^{66}Cu, electron capture decay of ^{66}Ga, elastic and inelastic scattering, as well as from reactions induced by light and heavy ions (see Ref. [26] and references therein).

In order to properly extract the electromagnetic matrix elements using the GOSIA code, it is recommended to consider the influence on the excitation process of at least one state above each of those observed in the experiment [25]. Introduction of these so-called "buffer states" provides means of accounting for virtual excitation of unobserved states and avoiding coupled-channel truncation effects. To this end, three buffer states were considered in ^{66}Zn: 4_2^+ (2766 keV), 4_3^+ (3576 keV), and (6_1^+) (4183 keV). The unobserved $4_1^+ \rightarrow 2_2^+$ transition was also included in the analysis; however, no buffer state above the 3_1^- level was declared. The only possible 2^+ state reported in the literature that could decay to the 0_2^+ state is located at 3882-keV excitation energy; however, the spin assignment of this level is only tentative [27] and the branching ratio for the transition populating the 0_2^+ state is

unknown. A hypothetical 2^+ state was therefore introduced in the present analysis in order to evaluate the possible impact of unobserved 2^+ states on the electromagnetic properties of the $0_2{}^+$ level. Its energy was estimated from the systematics of neighboring isotopes, taking into account also the available theoretical predictions. Furthermore, the influence of the excitation energy of this additional 2^+ state on matrix elements related to the $0_2{}^+$ level was tested by varying it in a wide range (3000–4000 keV).

The energy of the $2_3{}^+ \rightarrow 2_1{}^+$ transition (1741 keV) is relatively close to those of the $4_2{}^+ \rightarrow 2_1{}^+$ and $(6_1{}^+) \rightarrow 4_1{}^+$ transitions (1726 and 1733 keV, respectively). It was not possible to resolve this triplet under the present experimental conditions and the level of statistics collected in the corresponding energy range (see Fig. 3) precluded a γ-γ-particle coincidence analysis. Hence, simulations were performed using the GOSIA code in order to evaluate the relative contributions of these three transitions to the peak observed at around 1735 keV. The adopted transition probabilities from Ref. [26] were initially assumed, considering all possible combinations of matrix elements if more than one value was reported (i.e., for the $4_1{}^+ \rightarrow 2_1{}^+$ and $2_2{}^+ \rightarrow 2_1{}^+$ transitions). When only upper limits of the $B(E2)$ values were known (i.e., for transitions de-exciting the $4_2{}^+$ and $0_2{}^+$ states), both the limit and a value corresponding to the half of it were considered in the calculations. These simulations show that the $2_3{}^+ \rightarrow 2_1{}^+$ transition is at least two orders of magnitude more intense than the $4_2{}^+ \rightarrow 2_1{}^+$ transition, and four orders of magnitude more intense than the $(6_1{}^+) \rightarrow 4_1{}^+$ transition. The same conclusions were reached assuming the set of matrix elements extracted from the present experiment (Table II). This large intensity difference can be qualitatively explained by the fact that the $2_3{}^+$ state can be reached from the ground state via a single $E2$ transition, while the excitation of the $4_2{}^+$ and $6_1{}^+$ states requires two- and three-step excitation processes, respectively (the role of multipolarities higher than $E3$ in the excitation process is considered to be negligible). Consequently, all of the counts in the peak observed at the energy around 1735 keV were attributed to the $2_3{}^+ \rightarrow 2_1{}^+$ transition.

Known branching ratios, $E2/M1$ mixing ratios, and lifetimes of yrast and nonyrast states measured in previous experiments were included in the GOSIA analysis as additional spectroscopic data points (Table III), entering the multidimensional χ^2 fit in the same way as the γ-ray intensities measured in the present experiment. These complementary experimental data increased the sensitivity of the analysis to second-order effects, such as spectroscopic quadrupole moments and relative signs of matrix elements, as well as helped to correctly evaluate the influence of nonobserved transitions on the measured excitation cross sections.

The lifetime of the $2_1{}^+$ state was previously measured in Coulomb-excitation experiments, yielding values of 2.33(15) [14] and 2.25(14) ps [32], which are in good agreement with other values deduced from the (γ, γ') reactions (2.51(16) ps [33–36]), Doppler shift attenuation method (DSAM) measurements following Coulomb excitation (2.44(4) [37] and 2.43(5) ps [38]), (e, e') scattering (2.39(14) ps [39]), and DSAM following the ^{63}Cu$(\alpha, p\gamma)$ [40] and the $(\alpha, \alpha'\gamma)$ [41] reactions [1.9(12) and 2.2(10) ps, respectively]. A weighted average of all these values has been assumed in the present analysis.

The lifetimes of the $2_2{}^+$ state reported in the literature vary from 0.27(10) ps (DSAM, ^{63}Cu$(\alpha, p\gamma)$ [40,42]) through $1.2^{+0.5}_{-0.3}$ ps (DSAM, ^{64}Ni$(\alpha, 2n\gamma)$ [43–45]) to 2.5(7) ps (Coulomb excitation [14]). The lifetime of the $4_1{}^+$ state was measured in several experiments resulting in the following values: 0.27(9) ps (DSAM, ^{63}Cu$(\alpha, p\gamma)$ [40,42]), $0.25^{+0.07}_{-0.04}$ ps (DSAM, $(n, n'\gamma)$ [46–49]), 0.52(2) ps (Coulomb excitation [14]), and 1.1(2) ps (DSAM following Coulomb excitation [37]). Due to the large discrepancies of the $\tau(2_2{}^+)$, $\tau(4_1{}^+)$ values reported in the literature, none of them were used in the first stage of the present GOSIA analysis.

A weighted average of the values determined in (γ, γ') [50] and DSAM after $(n, n'\gamma)$ [49] was used for the lifetime of the $2_3{}^+$ state. The lifetime of the $3_1{}^-$ state was measured with DSAM following Coulomb excitation (0.260(10) ps [37]), $(\alpha, \alpha'\gamma)$ (0.26(6) ps [41]), ^{63}Cu$(\alpha, p\gamma)$ (0.33(20) ps [40,42]), and $(n, n'\gamma)$ (0.25(6) ps [49]). The weighted average of these values was assumed in the analysis.

The lifetime of the $(6_1{}^+)$ state was included as a weighted average of the values measured with DSAM following the ^{63}Cu$(\alpha, p\gamma)$ [40,42] and ^{64}Ni$(\alpha, 2n\gamma)$ [43–45]) reactions.

Only lower limits are available for the lifetimes of the $0_2{}^+$ and $4_2{}^+$ states ($>$0.30 ps and $>$10 ps, respectively [50]), and no value is reported for the $4_3{}^+$ state. Therefore, no lifetimes could be included in the present analysis for these three states.

The $2_3{}^+ \rightarrow 4_1{}^+/2_3{}^+ \rightarrow 0_1{}^+ = 11(3)\%$ branching ratio from Ref. [47] was not included, because assuming the $B(E2; 2_3{}^+ \rightarrow 0_1{}^+)$ value calculated from $\tau(2_3{}^+)$ would result in $B(E2; 2_3{}^+ \rightarrow 4_1{}^+) = 2600(700)$ W.u., indicating that this result is likely to be incorrect. The effect of the $4_3{}^+ \rightarrow 2_1{}^+$ and $4_3{}^+ \rightarrow 3_1^-$ transitions on the global fit was verified to be negligible; therefore, these two transitions were not included in the analysis.

Coulomb-excitation cross sections for all considered states are calculated in the GOSIA code taking into account the geometry of the GALILEO and SPIDER arrays. Positions (i.e., the polar and azimuthal angles with respect to the beam direction) and relative efficiencies of all 24 HPGe detectors forming the GALILEO array were used to account for the angular distribution of γ rays following Coulomb excitation. The attenuation of the γ-ray angular distribution due to physical sizes of the HPGe detectors and the deorientation effect during recoil into vacuum were also considered. The integration of the calculated Coulomb-excitation cross sections over the angular range covered by the particle detector required a full description of the SPIDER array in terms of polar and azimuthal angles covered by the particle detectors. During the experiment, one of the SPIDER detectors was disabled and one strip was powered off, resulting in an asymmetric shape of the particle detector. Furthermore, the off-centering of the beam spot with respect to the symmetry axis of the SPIDER array had to be taken into account. The description of the active particle detection surface in the GOSIA analysis was achieved by providing its boundaries in the (θ, ϕ) plane, as explained in Ref. [51]. An alternative approach was also tested: Each of the 47 individual SPIDER strips was described as a

TABLE II. Reduced $E2$, $E3$, and $M1$ matrix elements extracted in the present analysis, presented together with the corresponding reduced transition probabilities, $B(^{E}_{M}\lambda)$, and spectroscopic quadrupole moments, Q_s. The relative signs of the matrix elements obtained from the present analysis are given as well. When no sensitivity was achieved for a specific sign this is indicated as $\pm$. The signs were determined relative to those of the matrix elements listed without any sign, assumed to be positive (see the text). The present experimental results are compared with previous measurements, large-scale shell-model (SM) and beyond-mean-field (BMF) calculations.

	$\langle I_f \Vert E2 \Vert I_i \rangle$ (e fm^2)	$B(E2; I_i \to I_f)$ (W.u.)[a]					
$I_i \to I_f$	Present	Present	Previous	SM-I	SM-II	SM-III	BMF
$2_1^+ \to 0_1^+$	37.2[b]	17.5[b]	17.5(4)[c]	18	12	17	30
$2_2^+ \to 2_1^+$	53(10)	35(13)	41(14) [14] 330(130)[d]	14	11	12	45
$2_2^+ \to 0_1^+$	$\pm 0.48^{+0.05}_{-0.07}$	$0.0029^{+0.0006}_{-0.0008}$	0.004(18) [14] 0.032(12)[d]	0.050	0.59	0.68	0.018
$0_2^+ \to 2_2^+$	−5.1(10)	1.6(6)	<22[e]	0.10	1.5	3.1	16
$0_2^+ \to 2_1^+$	6.9(12)	3.0(10)	<40[e]	1.1	1.7	2.1	18
$4_1^+ \to 2_2^+$				2.7	3.2	3.9	0.031
$4_1^+ \to 2_1^+$	34(3)	8.1(12)	8.4(15) [37] 17.5(7) [14] 35(8)[f]	0.92	0.21	1.1	44
$4_2^+ \to 2_2^+$			<4[g]	0.011	0.18	0.4	22
$4_2^+ \to 2_1^+$			<0.13[g]	22	9.3	20	3.0
$2_3^+ \to 4_1^+$	±(25–60)	8–33	2600(700)[h]	0.31	0.068	6.4	6.7
$2_3^+ \to 2_2^+$	$+9^{+2}_{-5}$	$1.0^{+0.6}_{-1.1}$	0.40(3)[i]	0.72	0.30	0.9	3.1
$2_3^+ \to 2_1^+$	$2.7^{+1.2}_{-0.9}$	$0.09^{+0.08}_{-0.06}$	0.13^{+20}_{-13}[i]	0.40	0.41	0.3	1.2
$2_3^+ \to 0_1^+$	−6.4(5)	0.52(8)	0.54(15)[i]	0.97	0.012	1.0	0.071
$3_1^+ \to 2_2^+$				24	9.6	22	65
	$\langle I_f \Vert E3 \Vert I_i \rangle$ (e fm^3)	$B(E3; I_i \to I_f)$ (W.u.)[a]					
$3_1^- \to 0_1^+$	71^{+11}_{-16}	$2.8^{+0.8}_{-1.3}$	20(3) [57–59]	5.0			22
	$\langle I_f \Vert M1 \Vert I_i \rangle$ [μ_N]	$B(M1; I_i \to I_f)$ [W.u.][a]					
$2_2^+ \to 2_1^+$	$-0.18^{+0.03}_{-0.05}$	$0.0035^{+0.0012}_{-0.0020}$	0.004(3) [14] 0.056(23)[d]	0.00094	2.9×10^{-5}	0.008	0.0061
$2_3^+ \to 2_2^+$	+0.33(0.13)	0.012(7)	0.012(3)[i]	0.00011	0.0010	0.0014	3.5×10^{-5}
$2_3^+ \to 2_1^+$	$+0.14^{+0.13}_{-0.09}$	$0.0022^{+0.0013}_{-0.0011}$	0.0022(7)[i]	0.12	0.0084	0.10	0.0027
	$\langle I_i \Vert E2 \Vert I_i \rangle$ (e fm^2)	$Q_s(I_i)$ ($e$fm^2)					
$2_1^+ \to 2_1^+$	+32(12)	+24(9)	+24(8) [14] −8.1(13) [60]	−23	−14	−23	−9.2
$2_2^+ \to 2_2^+$	<0	<0		+21	+13	+20	+13
$4_1^+ \to 4_1^+$	>0	>0		+47	+38	−22	−26
$4_2^+ \to 4_2^+$				−29	−43	−21	−11
$3_1^+ \to 3_1^+$				−1.8	−1.0	−3.3	−0.23

[a]For ^{66}Zn: 1 W.u. ($E2$) = 15.84 e^2 fm^4, 1 W.u. ($E3$) = 258.8 e^2 fm^6, 1 W.u. ($M1$) = 1.790 μ_N^2.
[b]This quantity was used to normalize the Coulomb-excitation cross sections and, therefore, should not be considered as a result of the present analysis. For this reason, it is reported without error bars (see the text for further explanation).
[c]Deduced from the weighted average of $\tau(2_1^+)$ from Refs. [14,32–39], see the text for the values.
[d]Deduced from the average of the lifetimes measured in Refs. [40,42] (adopted value in Ref. [26]), $E2/M1$ mixing ratio from Ref. [15] (-1.6(2), adopted value in Ref. [26]) and branching ratios from Refs. [28,29], see the text for the values.
[e]Deduced from limits on widths measured in Ref. [50] and branching ratios from Refs. [28,29], see the text for the values.
[f]Deduced from the weighted average of $\tau(4_1^+)$ from Refs. [40,42,46–49], see the text for the values.
[g]Deduced from the $\tau(4_2^+)$ lower limit from Ref. [50] and branching ratios from Ref. [47], see the text for the values.
[h]Deduced from the average of the lifetimes measured in Refs. [49,50] (adopted value in Ref. [26]), $E2/M1$ mixing ratio from Ref. [15] and branching ratios from Refs. [28–30], see the text for the values.
[i]Deduced from the average of the lifetimes measured in Refs. [49,50] (adopted value in Ref. [26]), $E2/M1$ mixing ratio from Ref. [15] and branching ratios from Refs. [28,29], see the text for the values.

TABLE III. Known branching ratios, $E2/M1$ mixing ratios, and lifetimes included in the present GOSIA analysis (column 3) and their values calculated from the obtained set of reduced electromagnetic matrix elements reported in Table II (column 4).

Branching ratios			
Transitions	Energies (keV)	Literature (%)	GOSIA fit (%)
$2_2^+ \to 0_1^+/2_2^+ \to 2_1^+$	1873/834	0.39(3) [28,29]	0.38(19)
$0_2^+ \to 2_2^+/0_2^+ \to 2_1^+$	500/1333	0.41(10) [28,29]	0.40(20)
$4_2^+ \to 4_1^+/4_2^+ \to 2_2^+$	315/893	36(2) [47]	36[a]
$4_2^+ \to 2_1^+/4_2^+ \to 2_2^+$	1727/893	87(3) [47]	87[a]
$2_3^+ \to 4_1^+/2_3^+ \to 0_1^+$	329/2780		0.03–0.20
$2_3^+ \to 2_2^+/2_3^+ \to 0_1^+$	907/2780	17.7(12) [28,29]	20(3)
$2_3^+ \to 2_1^+/2_3^+ \to 0_1^+$	1741/2780	23.1(3) [28,29]	20(6)
$3_1^- \to 2_2^+/3_1^- \to 2_1^+$	954/1787	11.3(13) [30]	11[a]
$4_3^+ \to 2_3^+/4_3^+ \to 2_2^+$	796/1704	53(12) [28,29]	53[a]
$4_3^+ \to 2_1^+/4_3^+ \to 2_2^+$	2537/1704	93(20) [28,29]	93[a]

$E2/M1$ mixing ratios			
Transitions	Energies (keV)	Literature	GOSIA fit
$2_2^+ \to 2_1^+$	834	−2.08(4) [31]	−2.1(7)
$2_3^+ \to 2_2^+$	907	+0.13(24) [15]	+0.20(13)
$2_3^+ \to 2_1^+$	1741	+0.33(28) [15]	+0.3(3)

Lifetimes			
Level	Energy (keV)	Literature[b] (ps)	GOSIA fit (ps)
2_1^+	1039	2.42(3)	2.42[c]
2_2^+	1873		2.9(10)
0_2^+	2372		4.1(14)
4_1^+	2451		1.13(17)
2_3^+	2780	0.38(10)	0.42(6)
3_1^-	2827	0.260(10)	0.26[a]
(6_1^+)	4183	0.22(9)	0.23[a]

[a]This quantity should be considered as a parameter of the minimization procedure and not as a result of the present analysis. For this reason, it is reported without error bars (see the text for further explanation).

[b]Weighted average (see the text for further explanation).

[c]This quantity was used to normalize the Coulomb-excitation cross sections and, therefore, should not be considered as a result of the present analysis. For this reason, it is reported without error bars (see the text for further explanation).

circular detector positioned at the center-of-mass angle of the strip, with a radius fitted to obtain the same Rutherford cross section as in the previous description [51]. These two methods to include the SPIDER geometry in the GOSIA code provided fully consistent results in terms of reduced electromagnetic matrix elements.

The experimental γ-ray yields were normalized to the $2_1^+ \to 0_1^+$ transition intensity, as the $\tau(2_1^+)$ in ^{66}Zn is known with a high precision. They were also corrected for internal conversion using coefficients from the Band-Raman Internal Conversion Coefficents (BRICC) database [52]. The uncertainties of the relative efficiency calibration (1–3% depending on the γ-ray energy) were added in quadrature to the statistical uncertainties of the γ-ray yields. The evolution of excitation cross sections as a function of the interaction depth in the target, due to the beam nuclei slowing down in the target material, was also accounted for, assuming stopping powers calculated using the SRIM code [53].

The χ^2 minimization procedure was performed with 35 experimental yields, in addition to the set of 15 complementary spectroscopic data listed in Table III. A total of 28 matrix elements were free to be varied: 2 $E1$, 22 $E2$ (including 4 diagonal), 1 $E3$, and 3 $M1$. The resulting reduced electromagnetic matrix elements and the corresponding $B(^E_M\lambda)$ values are presented in Table II. As the $2_1^+ \to 0_1^+$ transition was used to normalize the Coulomb-excitation cross sections, it is not surprising that the $B(E2; 2_1^+ \to 0_1^+)$ value was perfectly reproduced by the fit (17.5 W.u.). However, the use of such normalization implies that this value [and the corresponding $\tau(2_1^+)$] cannot be considered to be an outcome of the present analysis and, consequently, it is not reported in Table II. The transitional and diagonal matrix elements are listed in Table II only if they are related to transitions directly observed, or if their extraction was possible by combining the γ-ray yields measured in the present experiment with previously known branching ratios, $E2/M1$ mixing ratios or lifetimes. For instance, the $B(E2; 0_2^+ \to 2_2^+)$ value could be determined since the $0_2^+ \to 2_1^+$ transition has been observed and the branching ratio $0_2^+ \to 2_2^+/0_2^+ \to 2_1^+$ is known. Similarly, by combining the measured $E1$ $3_1^- \to 2_1^+$ yield with the $3_1^- \to 2_2^+/3_1^- \to 2_1^+$ branching ratio, it was possible to determine the 3_1^- excitation cross section. In contrast to the electromagnetic decay of opposite parity states that proceeds predominantly via fast $E1$ transitions, Coulomb excitation of such states involves almost exclusively $E3$ and $E2$ transitions [54] and, consequently, the obtained cross section could be directly related to the $B(E3; 3_1^- \to 0_1^+)$ value. At the same time, the present experiment was not sensitive to $E1$ matrix elements, and their values in the fit were constrained by the known $\tau(3_1^-)$ value.

The statistical uncertainties were obtained by sampling the χ^2 surface and applying the $\chi^2_{\min} + 1$ condition around the minimum, corresponding to a 68.3% confidence limit on each matrix element. In this way, correlations between matrix elements were taken into account in the error estimation. Systematic effects related to uncertainties of the target thickness, beam energy, stopping powers, and geometrical description of SPIDER were found to be negligible. Only the uncertainty on the relative efficiencies of the HPGe detectors had an impact on the final uncertainties. In order to estimate the influence of the buffer states on the obtained set of matrix elements, the matrix elements involving the 4_2^+, 4_3^+ states were varied, while keeping the known branching ratios listed in Table III fixed. No significant effect has been observed. Also, the extracted matrix elements do not depend on the values of the $\langle 2_2^+||E2||4_1^+\rangle$ and $\langle 2_3^+||E2||2_3^+\rangle$ matrix elements, and the effect of the hypothetical 2^+ buffer state decaying to the 0_2^+ was found to be negligible within the obtained uncertainties. All the matrix elements that were not related to the γ-ray yields observed in the present experiment or to the additional spectroscopic data included in the analysis were, however, constrained during the GOSIA minimization by imposing a global upper limit for the intensities of related

γ-ray transitions [25]. This detection limit was estimated from the fluctuations in the experimental spectrum by applying the method of Ref. [55] to the high-background region below the $2_1^+ \rightarrow 0_1^+$ transition (see Fig. 3), at the energy of the $4_2^+ \rightarrow 2_2^+$ transition (893 keV).

Relative signs of $E2$ matrix elements may have a strong influence on multistep Coulomb-excitation cross sections [51,56]. The wave function of each state has an arbitrary phase that can be selected by fixing the sign of one matrix element involving this state, which ensures a consistent phase convention. The following sign convention has been imposed in the present analysis: Signs of all in-band transitional $E2$ matrix elements, both in the ground state and in the side bands (see Fig. 4), were assumed to be positive, as well as those of the $\langle 2_1^+||E2||2_2^+\rangle$, $\langle 2_1^+||E2||0_2^+\rangle$, $\langle 2_1^+||E2||2_3^+\rangle$, and $\langle 0_1^+||E3||3_1^-\rangle$ matrix elements. Signs of all remaining matrix elements were determined relative to those. Signs of the $M1$ matrix elements were given by the known $E2/M1$ mixing ratios. The obtained signs, presented in Table II, were verified by performing the χ^2 minimization with the same values of matrix elements but different signs, testing all possible combinations. When opposite signs with respect to the ones shown in Table II were imposed, a larger χ^2 value was found, exceeding the $\chi^2_{\text{min}} + 1$ condition. For the small $\langle 0_1^+||E2||2_2^+\rangle$ matrix element, the present measurement did not provide enough sensitivity to determine its relative sign, which is, in principle, relevant for the determination of the spectroscopic quadrupole moment $Q_s(2_1^+)$. Indeed, the sign of the following interference term

$$P_3 = \langle 0_1^+||E2||2_1^+\rangle\langle 2_1^+||E2||2_2^+\rangle\langle 2_2^+||E2||0_1^+\rangle$$

can, in general, influence the populations of the 2_1^+ and 2_2^+ states, which also depend on the quadrupole moments of these states. In order to evaluate the impact of this sign on the $Q_s(2_1^+)$ extracted from the present data, the $\langle 0_1^+||E2||2_2^+\rangle$ matrix element was varied within the limits given by the estimated error on its absolute value, covering a wide range of negative and positive values. This analysis indicated that the sign of $Q(2_1^+)$ is not affected by the sign of the $\langle 0_1^+||E2||2_2^+\rangle$ matrix element within the determined uncertainties. This is due to the small magnitude of the P_3 term in the present case, which does not impact the final $Q(2_1^+)$ value, consistent with the results of the previous Coulomb-excitation study of ^{66}Zn [14].

The $\tau(4_1^+)$ value obtained in this analysis [1.12(16) ps] was found to be in agreement with the lifetime reported in Ref. [37] [1.1(2) ps]. Hence, the value of Ref. [37] was included as an additional spectroscopic data point in the second phase of the analysis in order to enhance the sensitivity to the spectroscopic quadrupole moment of the 4_1^+ state. Even though no transitions decaying to that state were observed in the present experiment, a positive sign of the $\langle 4_1^+||E2||4_1^+\rangle$ diagonal matrix element was found, since an initial opposite sign was always restored to positive following the χ^2 minimization. A similar effect was observed for the sign of the $\langle 2_2^+||E2||2_2^+\rangle$ matrix element. Even though the $2_3^+ \rightarrow 2_1^+$ transition was observed and the $2_3^+ \rightarrow 2_2^+/2_3^+ \rightarrow 2_1^+$ branching ratio is known, it was not possible to determine the $Q_s(2_2^+)$ value due to the large uncertainties of the measured

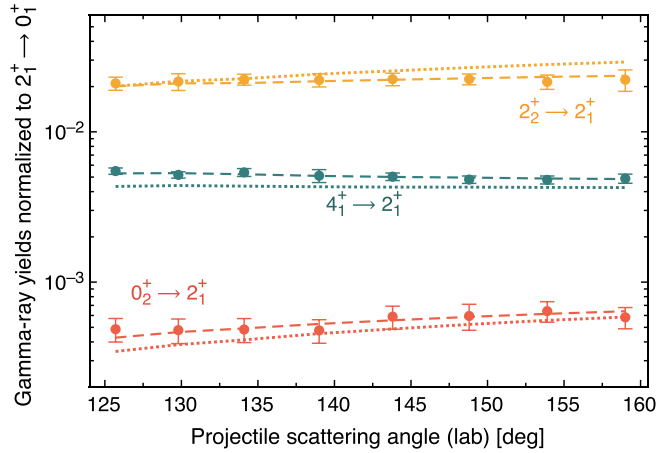

FIG. 5. Comparison between the γ-ray yields measured in the present experiment for the three most intense transitions (circles) and those calculated using the final set of reduced electromagnetic matrix elements resulting from the χ^2 minimization performed with the GOSIA code, listed in Table II (dashed lines). The calculated γ-ray yields for the local minimum obtained from a fit imposing opposite signs of the $Q_s(2_1^+)$, $Q_s(2_2^+)$, and $Q_s(4_1^+)$ quadrupole moments with respect to the ones of Table II (see the text for further information) are plotted with dotted lines. The calculated yields are integrated over the target thickness and the particle detector angular coverage. All yields are efficiency corrected and given relative to those of the $2_1^+ \rightarrow 0_1^+$ transition.

$2_3^+ \rightarrow 2_1^+$ yield and the fact that the influence of possible coupling to the 4_2^+ state on the excitation cross sections was not sufficiently constrained. However, it has been established that this quadrupole moment is negative: As in the case of the $Q_s(4_1^+)$, if the sign of the $\langle 2_2^+||E2||2_2^+\rangle$ matrix element was imposed to be positive, the minimization routine would always restore it to negative. Furthermore, even though the $\langle 4_1^+||E2||2_3^+\rangle$ matrix element was not constrained by any known branching ratio, it was possible to set lower and upper limits on its absolute value, as it was found to impact the calculated yields of the observed transitions. Only if the $\langle 4_1^+||E2||2_3^+\rangle$ matrix element was between the limits reported in Table II, the calculated χ^2 did not exceed the $\chi^2_{\text{min}} + 1$ condition.

Figure 5 shows a comparison between the measured γ-ray yields (efficiency-corrected and normalized to the $2_1^+ \rightarrow 0_1^+$ yield) and those calculated from the obtained set of matrix elements for the three most intense transitions, represented with dashed lines. An agreement within 1σ uncertainty is obtained for the whole angular range. For the $2_3^+ \rightarrow 2_1^+$, $3_1^- \rightarrow 2_1^+$, and $2_2^+ \rightarrow 0_1^+$ transitions, analyzed in coincidence with the full SPIDER detector, the γ-ray yields calculated by the GOSIA code are equal to 1.8×10^{-5}, 6.0×10^{-5}, and 7.3×10^{-5}, respectively (also in this case efficiency-corrected and normalized to the $2_1^+ \rightarrow 0_1^+$ yield). When compared with the values presented in Table I, an agreement within 1σ uncertainty is found, except for the $2_3^+ \rightarrow 2_1^+$ yield, which agrees with the experimental value within 2σ.

For comparison, Fig. 5 also shows the calculated yields for the $2_2^+ \rightarrow 2_1^+$, $4_1^+ \rightarrow 2_1^+$, and $0_2^+ \rightarrow 2_1^+$ transitions

when opposite signs of the $Q_s(2_1^+)$, $Q_s(2_2^+)$, and $Q_s(4_1^+)$ quadrupole moments are imposed with respect to the ones of Table II. Such combination of signs of the quadrupole moments provides a better reproduction of the measured γ-ray intensities and spectroscopic data than, for example, a solution where the signs of $Q_s(2_1^+)$ and $Q_s(4_1^+)$ are different, or where those of $Q_s(2_1^+)$ and $Q_s(2_2^+)$ are identical. However, the total χ^2 for the corresponding local minimum exceeds by ≈3.5 the value obtained for the global minimum, i.e., the solution presented in Table II. This is mostly related to a worse reproduction of the angular dependence of the γ-ray yields, in particular for the $2_2^+ \rightarrow 2_1^+$ transition. Additionally, this solution yields the lifetime of the 2_2^+ state close to 10 ps, which is not consistent with any of the previous measurements.

As shown in Table III, the final set of reduced electromagnetic matrix elements reproduces all the spectroscopic data included in the present analysis within 1σ uncertainty. Those related to the buffer states cannot be considered as an output of the present analysis, as these states were not observed and they had no influence on the measured yields. They should rather be seen as parameters of the minimization procedure, which is bound to reproduce them. Therefore, their values resulting from the GOSIA fit are reported without error bars in Table III. Similarly, as the present experiment was not sensitive to $E1$ matrix elements, the $\tau(3_1^-)$ and the $3_1^- \rightarrow 2_2^+/3_1^- \rightarrow 2_1^+$ branching ratio resulting from the fit cannot be considered as outcomes of the analysis.

IV. DISCUSSION

The $B(^E_M\lambda)$ values deduced from the set of matrix elements presented in Table II are in good agreement with the values obtained in the previous measurements, except for $B(E3; 3_1^- \rightarrow 0_1^+)$ (here it should be noted that both previous studies [58,59] used a fundamentally different method to determine this quantity, i.e., electron scattering) and the limits of the $B(E2; 2_3^+ \rightarrow 4_1^+)$ value. When more than one value was available in the literature, the achieved precision allows for the discrimination between them. The $B(E2)$ values for transitions de-populating the 0_2^+ state and, consequently, its lifetime have been deduced for the first time, and they are compatible with the limits reported in the literature. Furthermore, relative signs for the $\langle 0_2^+||E2||2_2^+\rangle$, $\langle 2_3^+||E2||2_2^+\rangle$, and $\langle 2_3^+||E2||0_1^+\rangle$ matrix elements have been determined, in addition to the signs of the spectroscopic quadrupole moments of the 2_2^+ and 4_1^+ states.

The extracted $Q_s(2_1^+)$ value indicates a moderate deformation and is in excellent agreement with the previous Coulomb-excitation result [14], being, however, three times larger in terms of magnitude than the value obtained from an electron scattering measurement [60]. A systematic discrepancy between the values obtained in Coulomb-excitation and electron-scattering experiments is apparent from Fig. 6, particularly regarding the sign of the $Q_s(2_1^+)$ [negative for ^{64,66,68}Zn from (e, e') measurements, while positive for ^{66,68}Zn and compatible with zero in ^{64}Zn from Coulomb excitation]. The deduced sign of the $Q_s(4_1^+)$ is the same as that of $Q_s(2_1^+)$, while the $Q_s(2_2^+)$ has an opposite sign. This is in agreement with what would be expected for a rigid rotor, assuming $K = 2$ for the 2_2^+ state. Although a rotational interpretation may not be the most appropriate for the ^{66}Zn isotope, it is worth noticing that the signs of spectroscopic quadrupole moments deduced from the present analysis agree with it, supporting a positive sign of $Q_s(2_1^+)$.

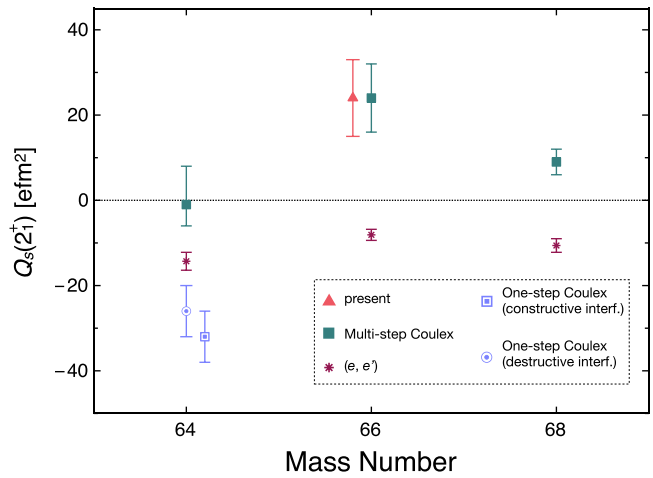

FIG. 6. Systematics of the experimental $Q_s(2_1^+)$ values in Zn isotopes with $N = 34$–38. The results of the present experiment are compared with those resulting from other measurements [14,60,62]. For clarity, some values are slightly offset on the X axis.

The resulting reduced transition probabilities for transitions depopulating the 2_2^+ state are in good agreement with those of Ref. [14]. The exceptionally large $B(E2; 2_2^+ \rightarrow 2_1^+) = 330(130)$ W.u. adopted in Ref. [26] would be difficult to explain, especially in the context of the existing systematics in light Zn isotopes [see Fig. 7(a)]. Instead, the presently extracted value is close to those observed in ^{64}Zn and ^{68}Zn, which indicate a moderately collective character of the 2_2^+ states. The relatively large uncertainties for the transitions depopulating the 2_2^+ state reflect strong correlations of the corresponding matrix elements with the $Q_s(2_1^+)$ value (observed also in Ref. [14]). Furthermore, the uncertainty of the $2_2^+ \rightarrow 2_1^+$ transition yield is affected by the fact that the corresponding peak is located on the Compton edge of the much more intense $2_1^+ \rightarrow 0_1^+$ transition. The systematic uncertainty resulting from the fit was carefully evaluated using the GEANT4 simulation code [17,61] and included in the value reported in Table I.

The extracted $B(E2; 0_2^+ \rightarrow 2_2^+)$ and $B(E2; 0_2^+ \rightarrow 2_1^+)$ values are small and of similar magnitude. The latter is consistent with the data available for the neighboring isotopes, exhibiting an almost exponential increase from ^{64}Zn to ^{70}Zn, as shown in Fig. 7(b). The description of the neighboring ^{64}Zn as a nucleus possessing $E(5)$ symmetry was explored by using the IBM [63], and it was suggested that the 0_2^+ states in ^{66,68}Zn could also be identified as the 0_ξ^+ states predicted within this approach. The obtained value of the $B(E2; 0_2^+ \rightarrow 2_2^+)/B(E2; 0_2^+ \rightarrow 2_1^+)$ ratio, 0.5(3), is indeed close to theoretical predictions for a 0_ξ^+ state (0.12) and rules out the interpretations of the 0_2^+ state as a partner of a γ-unstable structure (for which the ratio should

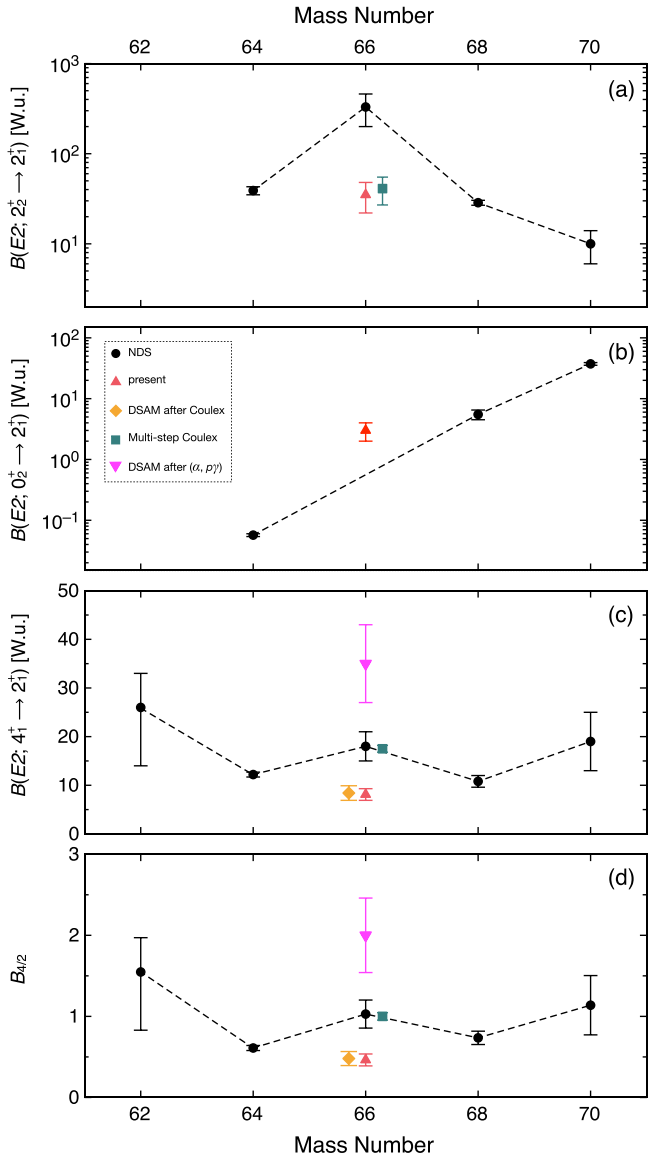

FIG. 7. Systematics of the adopted [26] experimental $B(E2; 2_2^+ \rightarrow 2_1^+)$, $B(E2; 0_2^+ \rightarrow 2_1^+)$, $B(E2; 4_1^+ \rightarrow 2_1^+)$, and $B_{4/2}$ values in Zn isotopes with $N = 32$–40 [note the logarithmic scale for panels (a) and (b)]. For ^{66}Zn, the results of the present experiment are also shown and compared with those resulting from other measurements [14,37,40]. The adopted values are connected by dashed lines. For clarity, some values are slightly offset on the X axis.

go to infinity) or a member of a vibrational-like structure (which would imply this ratio equal to 0). However, in the model reported in Ref. [63], a value of 0.49 was predicted for the $B(E2; 0_2^+ \rightarrow 2_1^+)/B(E2; 2_1^+ \rightarrow 0_1^+)$ ratio, while the present experimental results yield 0.17(6). Combining the $\tau(0_2^+)$ value deduced from the measured matrix elements with the $X(E0/E2)$ value measured in Ref. [10], the monopole transition strength $\rho^2(E0; 0_2^+ \rightarrow 0_1^+) \times 10^3 = 4.0(15)$ can be extracted. This value is similar to those measured in ^{64}Zn ($\rho^2(E0; 0_2^+ \rightarrow 0_1^+) \times 10^3 = 3.8(4)$ [10]) and in ^{68}Zn ($\rho^2(E0; 0_2^+ \rightarrow 0_1^+) \times 10^3 = 7(4)$ [10]). It indicates a similar deformation of the 0_1^+ and 0_2^+ states or/and a small mixing between them.

The $B(E2; 4_1^+ \rightarrow 2_1^+)$ value obtained in the present analysis is in agreement with the lowest of the previously measured values. The corresponding $B_{4/2} = B(E2; 4_1^+ \rightarrow 2_1^+)/B(E2; 2_1^+ \rightarrow 0_1^+) = 0.46(7)$ ratio indicates low collectivity of the 4_1^+ state. Interestingly, anomalously low $B_{4/2} < 1$ values are also known in the ^{64}Zn and ^{68}Zn isotopes [see Fig. 7(d)] and in ^{74}Zn [64].

Although the experimental quantities obtained in the present analysis confirm the collective character of ^{66}Zn, their pattern prevents drawing a consistent picture of the low-lying states within any simplified geometrical approach. Hence, the extracted set of matrix elements was analyzed using the quadrupole sum rules method, in order to investigate the role of triaxiality in the ^{66}Zn ground state and the deformation of the 0_2^+ state. Furthermore, new microscopic calculations using beyond-mean-field (BMF) and large-scale shell-model (SM) approaches were performed and confronted with the obtained experimental results.

A. Quadrupole sum rules

The quadrupole sum rules method can provide information on the charge distribution of the investigated nucleus in its specific states. It is based on the fact that the electric quadrupole operator, $E2$, is a spherical tensor and thus its zero-coupled products are rotationally invariant. Such invariants can be linked to deformation parameters in the intrinsic frame of the nucleus, namely Q, the overall quadrupole deformation parameter (equivalent to the elongation parameter β in the Bohr's model) and δ, which is related to the triaxiality parameter γ. The lowest order shape invariant, $\langle Q^2 \rangle$, is proportional to the sum of squared $E2$ matrix elements $\langle i||E2||t\rangle\langle t||E2||i\rangle$ over all intermediate states $|t\rangle$ that can be reached from the state $|i\rangle$ with a single $E2$ transition:

$$\langle i||Q^2||i\rangle = \frac{\sqrt{5}}{\sqrt{2I_i+1}} \sum_t M_{it} M_{ti} \begin{Bmatrix} 2 & 2 & 0 \\ I_i & I_i & I_t \end{Bmatrix}, \quad (1)$$

where $M_{ab} = \langle a||E2||b\rangle$, I_i is the spin of the state i, and $\{\}$ is Wigner's 6-j symbol. The next-order invariant, $\langle Q^3 \cos(3\delta)\rangle$, is constructed from triple products of $E2$ matrix elements, $\langle i||E2||t\rangle\langle t||E2||u\rangle\langle u||E2||i\rangle$, where $|i\rangle$ is the state in question and $|t\rangle$ and $|u\rangle$ are the intermediate states:

$$\langle i||Q^3 \cos(3\delta)||i\rangle = \mp\sqrt{\frac{35}{2}} \frac{1}{2I_i+1} \sum_{tu} M_{iu} M_{ut} M_{ti} \begin{Bmatrix} 2 & 2 & 2 \\ I_i & I_t & I_u \end{Bmatrix}, \quad (2)$$

where the negative sign corresponds to an integral spin system, while a positive sign should be used for a half-integral spin system. The diagonal matrix elements (i.e., $|t\rangle = |u\rangle$), including their signs, have to be known in order to extract this shape invariant, as well as the relative signs of all relevant transitional matrix elements. The relations $\langle Q^2 \rangle = q_0^2 \langle \beta^2 \rangle$ and $\langle Q^3 \cos(3\delta)\rangle = q_0^3 \langle \beta^3 \cos(3\gamma)\rangle$ (where $q_0 = \frac{3}{4\pi} ZR^2$) can be used to calculate the β and γ collective shape parameters from the shape invariants, assuming $\langle \beta \rangle \approx \sqrt{\langle \beta^2 \rangle}$ and

TABLE IV. $\langle Q^2\rangle$ quadrupole shape invariants for the $0^+_{1,2}$ and 2^+_1 states in ^{66}Zn, calculated using experimental and theoretical values of $E2$ matrix elements. All products of matrix elements contributing to the final values of $\langle Q^2\rangle$ are listed. The invariants are formed by summing all products of matrix elements and then multiplying the sum by a spin factor, equal to 1 for the $0^+_{1,2}$ states, and to 1/5 in the case of the 2^+_1 state [see Eq. (1)].

State	Component $E2\times E2$	Contribution to $\langle Q^2\rangle$ [e^{2}b^2] Experiment	SM-I	SM-II	SM-III	BMF
$0_1{}^+$	$\langle 0_1{}^+\|\|E2\|\|2_1{}^+\rangle\langle 2_1{}^+\|\|E2\|\|0_1{}^+\rangle$	0.14	0.14	0.094	0.14	0.24
	$\langle 0_1{}^+\|\|E2\|\|2_2{}^+\rangle\langle 2_2{}^+\|\|E2\|\|0_1{}^+\rangle$	2.3×10^{-5}	3.9×10^{-4}	4.7×10^{-3}	5.3×10^{-3}	1.0×10^{-4}
	$\langle 0_1{}^+\|\|E2\|\|2_3{}^+\rangle\langle 2_3{}^+\|\|E2\|\|0_1{}^+\rangle$	4.2×10^{-3}	7.7×10^{-3}	1.2×10^{-4}	8.3×10^{-3}	6.1×10^{-4}
	$\langle Q^2\rangle$	0.143(8)	0.15	0.098	0.15	0.24
	$\langle\beta\rangle$	0.224(6)	0.23	0.19	0.23	0.30
$2_1{}^+$	$\langle 2_1{}^+\|\|E2\|\|0_1{}^+\rangle\langle 0_1{}^+\|\|E2\|\|2_1{}^+\rangle$	0.14	0.14	0.094	0.14	0.24
	$\langle 2_1{}^+\|\|E2\|\|0_2{}^+\rangle\langle 0_2{}^+\|\|E2\|\|2_1{}^+\rangle$	4.8×10^{-3}	1.8×10^{-3}	2.7×10^{-3}	3.4×10^{-3}	0.028
	$\langle 2_1{}^+\|\|E2\|\|2_2{}^+\rangle\langle 2_2{}^+\|\|E2\|\|2_1{}^+\rangle$	0.28	0.11	0.088	0.093	0.36
	$\langle 2_1{}^+\|\|E2\|\|2_3{}^+\rangle\langle 2_3{}^+\|\|E2\|\|2_1{}^+\rangle$	7.0×10^{-4}	3.2×10^{-3}	3.2×10^{-3}	2.4×10^{-3}	9.5×10^{-3}
	$\langle 2_1{}^+\|\|E2\|\|4_1{}^+\rangle\langle 4_1{}^+\|\|E2\|\|2_1{}^+\rangle$	0.12	0.013	3.0×10^{-3}	0.016	0.62
	$\langle 2_1{}^+\|\|E2\|\|4_2{}^+\rangle\langle 4_2{}^+\|\|E2\|\|2_1{}^+\rangle$		0.31	0.13	0.28	0.042
	$\langle 2_1{}^+\|\|E2\|\|4_3{}^+\rangle\langle 4_3{}^+\|\|E2\|\|2_1{}^+\rangle$		7.3×10^{-3}	0.021	6.9×10^{-3}	1.5×10^{-3}
	$\langle 2_1{}^+\|\|E2\|\|3_1{}^+\rangle\langle 3_1{}^+\|\|E2\|\|2_1{}^+\rangle$		1.7×10^{-3}	6.6×10^{-3}	8.9×10^{-3}	4.9×10^{-4}
	$\langle 2_1{}^+\|\|E2\|\|2_1{}^+\rangle\langle 2_1{}^+\|\|E2\|\|2_1{}^+\rangle$	0.10	0.090	0.032	0.09	1.5×10^{-3}
	$\langle Q^2\rangle$	0.13(3)	0.14	0.077	0.13	0.26
	$\langle\beta\rangle$	0.21(3)	0.22	0.16	0.21	0.30
$0_2{}^+$	$\langle 0_2{}^+\|\|E2\|\|2_1{}^+\rangle\langle 2_1{}^+\|\|E2\|\|0_2{}^+\rangle$	4.8×10^{-3}	1.8×10^{-3}	2.7×10^{-3}	3.4×10^{-3}	0.028
	$\langle 0_2{}^+\|\|E2\|\|2_2{}^+\rangle\langle 2_2{}^+\|\|E2\|\|0_2{}^+\rangle$	2.6×10^{-3}	2.1×10^{-4}	2.3×10^{-3}	4.8×10^{-3}	0.023
	$\langle Q^2\rangle$	$7.4(19)\times10^{-3}$	2.0×10^{-3}	5.0×10^{-3}	8.2×10^{-3}	0.054
	$\langle\beta\rangle$	0.051(7)	0.026	0.042	0.054	0.14

$\langle\beta^3\cos(3\gamma)\rangle \approx \langle\beta^2\rangle^{3/2}\langle\cos(3\gamma)\rangle$ [65,66]. A detailed description of the quadrupole sum rules method can be found in Refs. [16,18,65–68].

The present experiment yielded a set of $E2$ matrix elements sufficient to determine the $\langle Q^2\rangle$ and $\langle Q^3\cos(3\delta)\rangle$ quadrupole shape invariants for the ground state (Tables IV and V). Although the $\langle 2_2{}^+||E2||2_2{}^+\rangle$ and $\langle 2_3{}^+||E2||2_3{}^+\rangle$ diagonal matrix elements could not be determined, their contribution was found to be negligible, as they enter the sum multiplied by the $\langle 0_1{}^+||E2||2_2{}^+\rangle$ and $\langle 0_1{}^+||E2||2_3{}^+\rangle$ matrix elements, respectively, which are small in ^{66}Zn. Similarly, the effect of the unknown sign of the $\langle 0_1{}^+||E2||2_2{}^+\rangle$ matrix element is negligible due to its small absolute value. In agreement with the existing systematics [69], the $\langle Q^3\cos(3\delta)\rangle$ invariant for the ground state is dominated by the following triple product:

$$\langle 0_1{}^+||E2||2_1{}^+\rangle\langle 2_1{}^+||E2||2_1{}^+\rangle\langle 2_1{}^+||E2||0_1{}^+\rangle.$$

The obtained values of $\langle Q^2\rangle$ and $\langle Q^3\cos(3\delta)\rangle$ indicate a moderate triaxial-oblate deformation of the ^{66}Zn ground state.

The overall deformation of the first excited $2_1{}^+$ state was also extracted, as shown in Table IV, and found to be close to the value obtained for the ground state in ^{66}Zn. Here, however, more matrix elements are missing (namely $\langle 2_1{}^+||E2||4_2{}^+\rangle$, $\langle 2_1{}^+||E2||4_3{}^+\rangle$, $\langle 2_1{}^+||E2||3_1{}^+\rangle$) and, therefore, the extracted value should be considered a lower limit of the overall deformation parameter. In particular, the theoretical calculations consistently indicate an important contribution of the $\langle 2_1{}^+||E2||4_2{}^+\rangle$ matrix element to the $\langle Q^2\rangle$ invariant. The contribution of higher lying states to the quadrupole invariants for the $0_1{}^+$ and $2_1{}^+$ states can be considered negligible with respect to those listed in Tables IV and V, as no other strong $E2$ decays feeding the states of interest are reported in the literature. This is further supported by the fact that in the theoretical calculations the contributions of the products involving the $2_4{}^+$, $3_1{}^+$, and $4_3{}^+$ states are at the level, at most, of a few percent of the total $\langle Q^2\rangle$ invariant.

The overall deformation of the $0_2{}^+$ state could be determined from the $\langle 0_2{}^+||E2||2_2{}^+\rangle$ and $\langle 0_2{}^+||E2||2_1{}^+\rangle$ matrix elements extracted in the present analysis. The obtained $\langle Q^2\rangle$ value indicates a much smaller deformation of the $0_2{}^+$ state with respect to the ground state. It should be noted that, apart from the above-mentioned state at 3883 keV with a tentative spin assignment 2^+, no other higher lying 2^+ states are known to decay to the $0_2{}^+$. However, a contribution from them to the $\langle Q^2\rangle$ invariant cannot be firmly excluded from the present experiment. Therefore, the value here deduced should again be considered to be a lower limit.

The level of mixing between the $0_1{}^+$ and $0_2{}^+$ states can be extracted in the framework of the phenomenological two-

TABLE V. $\langle 0_1{}^+|Q^3\cos(3\delta)|0_1{}^+\rangle$ quadrupole shape invariant calculated using experimental and theoretical values of $E2$ matrix elements in ^{66}Zn. All triple products of matrix elements contributing to $\langle 0_1{}^+|Q^3\cos(3\delta)|0_1{}^+\rangle$ are listed. The invariant is formed by summing all triple products and then multiplying the sum by a spin factor of -0.837 [see Eq. (2)]. An additional factor of two is applied to the products of three transitional matrix elements, as they can be formed in two possible ways (e.g., $\langle 0_1{}^+||E2||2_1{}^+\rangle\langle 2_1{}^+||E2||2_2{}^+\rangle\langle 2_2{}^+||E2||0_1{}^+\rangle$ and $\langle 0_1{}^+||E2||2_2{}^+\rangle\langle 2_2{}^+||E2||2_1{}^+\rangle\langle 2_1{}^+||E2||0_1{}^+\rangle$).

State	Component $E2\times E2\times E2$	Contribution to $\langle Q^3\cos(3\delta)\rangle$ [e^{3}b^3] Experiment	SM-I	SM-II	SM-III	BMF
$0_1{}^+$	$\langle 0_1{}^+\|\|E2\|\|2_1{}^+\rangle\langle 2_1{}^+\|\|E2\|\|2_1{}^+\rangle\langle 2_1{}^+\|\|E2\|\|0_1{}^+\rangle$	$+0.045$	-0.042	-0.017	-0.041	-0.029
	$\langle 0_1{}^+\|\|E2\|\|2_2{}^+\rangle\langle 2_2{}^+\|\|E2\|\|2_2{}^+\rangle\langle 2_2{}^+\|\|E2\|\|0_1{}^+\rangle$	-7.0×10^{-6}	$+1.1\times10^{-4}$	$+7.8\times10^{-4}$	$+1.4\times10^{-3}$	$+2.4\times10^{-5}$
	$\langle 0_1{}^+\|\|E2\|\|2_3{}^+\rangle\langle 2_3{}^+\|\|E2\|\|2_3{}^+\rangle\langle 2_3{}^+\|\|E2\|\|0_1{}^+\rangle$	$+1.2\times10^{-3}$	-2.1×10^{-3}	-1.7×10^{-5}	-1.2×10^{-3}	-8.8×10^{-5}
	$\langle 0_1{}^+\|\|E2\|\|2_1{}^+\rangle\langle 2_1{}^+\|\|E2\|\|2_2{}^+\rangle\langle 2_2{}^+\|\|E2\|\|0_1{}^+\rangle$	$\pm9.3\times10^{-4}$	$+5.0\times10^{-3}$	$+0.012$	$+8.2\times10^{-3}$	$+3.4\times10^{-3}$
	$\langle 0_1{}^+\|\|E2\|\|2_1{}^+\rangle\langle 2_1{}^+\|\|E2\|\|2_3{}^+\rangle\langle 2_3{}^+\|\|E2\|\|0_1{}^+\rangle$	-6.6×10^{-4}	-3.7×10^{-3}	-3.4×10^{-4}	-1.7×10^{-3}	-1.1×10^{-3}
	$\langle 0_1{}^+\|\|E2\|\|2_2{}^+\rangle\langle 2_2{}^+\|\|E2\|\|2_3{}^+\rangle\langle 2_3{}^+\|\|E2\|\|0_1{}^+\rangle$	-2.7×10^{-5}	-2.6×10^{-4}	-6.5×10^{-5}	$+5.6\times10^{-4}$	$+4.4\times10^{-5}$
	$\langle Q^3\cos(3\delta)\rangle$	$-0.039(14)$	$+0.036$	$+3.4\times10^{-3}$	$+0.023$	$+0.020$
	$\langle\cos(3\delta)\rangle$	$-0.7(3)$	$+0.6$	$+0.1$	$+0.4$	$+0.2$
	$\langle\gamma\rangle$	$44(8)^\circ$	17°	28°	22°	27°

state mixing model (see Ref. [70] and the references therein). Assuming that the observed physical states can be expressed as linear combinations of two pure structures, their mixing is quantified by an angle, θ_0. Following the procedure of Ref. [68], by combining the $\rho^2(E0;0_2{}^+\rightarrow 0_1{}^+)$ value with the deformation parameters for the $0_1{}^+$ and $0_2{}^+$ states deduced in the present work, $\cos^2(\theta_0)=0.968(14)$ was determined, indicating almost pure configurations of the wave functions of the discussed two 0^+ states. Although the γ deformation parameter could not be extracted for the $0_2{}^+$ state, the effect of the nonaxial degree of freedom on the $\cos^2(\theta_0)$ value was found to be negligible within the experimental uncertainties, because the overall deformation of the $0_2{}^+$ state is small compared to that of the $0_1{}^+$ state

The deformation parameters Q and δ extracted using the sum rules method represent the mean value of the nuclear deformation in a given state. Higher order shape invariants would have to be considered in order to estimate possible shape dispersions. In the present experiment, the set of extracted matrix elements is insufficient to make such analysis for any of the observed states. Therefore, it should be kept in mind that the reported $\langle\beta\rangle$ and $\langle\gamma\rangle$ values should not be interpreted as measures of a static deformation, and the nuclear wave functions may exhibit large fluctuations around these mean values, as discussed in Refs. [68,71].

B. Beyond-mean-field calculations

The intrinsic shapes of the low-lying states in ^{66}Zn were further interpreted in the framework of microscopic calculations performed in a self-consistent beyond mean-field theory. The symmetry-conserving configuration mixing (SCCM) method [72] was applied using the Gogny D1S interaction [73]. Within this method, the intrinsic states are described as Hartree-Fock-Bogoliubov (HFB)–like wave functions obtained self-consistently through particle-number variation after projection (PN-VAP) [74]. The wave functions are expressed as linear combinations of particle number and angular momentum projected mean-field states, with the coefficients calculated following the generator coordinate method (GCM) [75].

The PN-VAP energies defined in the (β_2,γ) plane for each of the stable Zn isotopes are shown in Fig. 8. The importance of the triaxial degree of freedom is apparent in all the isotopes, and it is even more evident after projecting the HFB states onto angular momentum $J=0$, as shown in Fig. 9 for ^{66}Zn. As seen in this figure, the ground state is characterized by a triaxial shape with a finite dispersion around $\gamma=30^\circ$.

The calculated level scheme agrees well with the experimental one, as shown in Fig. 10. By including the shape

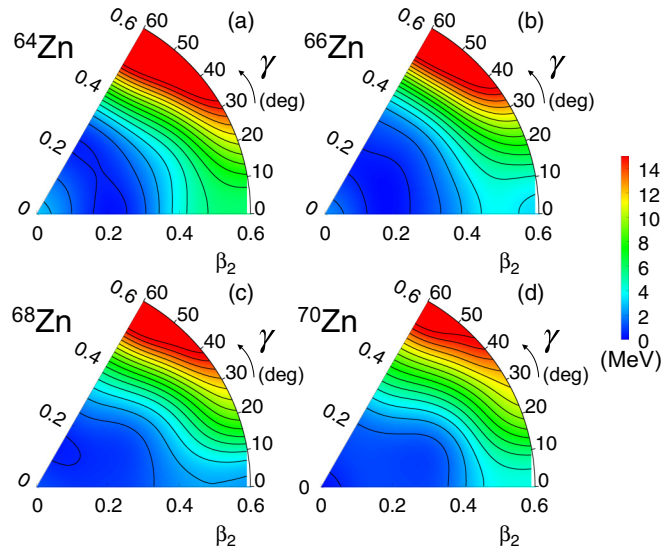

FIG. 8. Potential energy surfaces for stable Zn isotopes resulting from deformation-constrained Hartree-Fock calculations with the particle number projection method (PN-VAP) and Gogny D1S interaction.

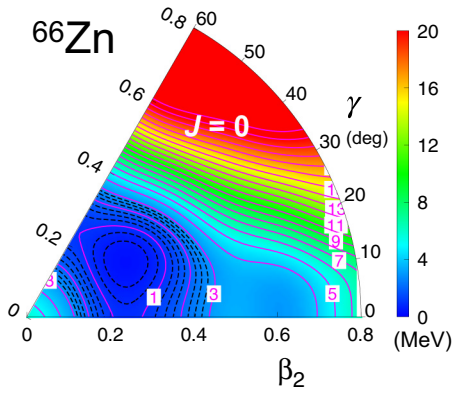

FIG. 9. Same as Fig. 8 for ^{66}Zn after projecting onto angular momentum $J = 0$. A triaxial shape with a finite dispersion characterize the isotope and a second prolate minimum results from the calculation.

mixing in the calculations, it is possible to describe the intrinsic shape of each state through collective wave functions (CWF) obtained within the SCCM framework, which represent the weights of (β_2, γ) deformation for each considered state. States with similar CWFs can then be grouped into bands, as proposed in Fig. 11. Two excited 0^+ states are predicted at 2181 and 2989 keV: The first one is a bandhead of a structure that has a slightly more oblate shape with respect to those built on the ground state and on the $2_2{}^+$ state (that resembles the bandhead of a γ band related to nonaxial rotation) and is characterized by a finite dispersion in the β_2 parameter toward the zero deformation. In contrast, a well-deformed prolate structure is predicted on top of the $0_3{}^+$ state. The mixing of structures built on $0_2{}^+$ and $0_3{}^+$ states is evidenced by the CWFs for the $2_3{}^+$ and $2_4{}^+$ states.

A set of reduced $E2$ and $M1$ electromagnetic matrix elements was extracted within the BMF framework. The resulting $B(E2)$, $B(M1)$, and Q_s values are compared to the experimental findings in Table II. The calculated $B(E2)$ values are generally larger than the experimental ones, with the exception of those related to the $2_3{}^+$ state. An enhanced quadrupole collectivity with respect to the experimental data is, therefore, predicted. In particular, the calculated $B_{4/2} = 1.47$ ratio is close to the value for a rigid axially symmetric rotor (equal to 1.43), while the experimental $B(E2)$ values obtained in the present work yield $B_{4/2} = 0.46(7)$. This large value of $B(E2; 4_1^+ \rightarrow 2_1^+)$ could potentially be reduced by the inclusion of time-reversal symmetry-breaking terms in the SCCM method that would produce a larger mismatch between the K components of the two states involved in this transition [76]. However, the computational cost of including cranking states is prohibitive, making this development beyond the scope of the present work [77]. In contrast, the $B(M1)$ values are well reproduced, with an exception of the $B(M1; 2_3{}^+ \rightarrow 2_2{}^+)$ underestimated by three orders of magnitude.

A negative sign of the $Q_s(2_1{}^+)$ value is predicted, which is in disagreement with the positive value determined in the present measurement but in agreement with that of Ref. [60]. In addition, opposite signs of the $Q_s(2_2{}^+)$ and $Q_s(4_1{}^+)$ quadrupole moments are predicted. However, the large dispersion of the CWFs around $\gamma = 30^\circ$ suggests that the signs of the spectroscopic quadrupole moments may not be as useful to assess the deformation of ^{66}Zn as they would be in genuine axial cases. Figure 12 shows the $Q_s(2_1{}^+)$ calculated as a function of the (β_2, γ) parameters. In the vicinity of $\gamma = 30^\circ$, the sign and magnitude of the spectroscopic quadrupole moment varies rapidly, going from positive values for $\gamma > 30^\circ$ to negative ones for $\gamma < 30^\circ$. Due to its triaxial character, the CWF for the $2_1{}^+$ state is mostly localized within the $-20\,e\,\mathrm{fm}^2 \lesssim Q_s \lesssim +20\,e\,\mathrm{fm}^2$ range, which is consistent with the experimental value obtained in the present work.

Furthermore, the quadrupole sum rules method was applied to the calculated set of matrix elements in order to extract the shape invariants following the same procedures that were used for the experimental matrix elements (see Tables IV and V). The BMF calculations confirm that the $\langle Q^2 \rangle$ and $\langle Q^3 \cos(3\delta) \rangle$ invariants for the ground state are dominated by the $\langle 0_1{}^+ || E2 || 2_1{}^+ \rangle \langle 2_1{}^+ || E2 || 0_1{}^+ \rangle$ and $\langle 0_1{}^+ || E2 || 2_1{}^+ \rangle \langle 2_1{}^+ || E2 || 2_1{}^+ \rangle \langle 2_1{}^+ || E2 || 0_1{}^+ \rangle$ products, respectively. The overall deformation predicted for the ground state is larger than that deduced from the experiment, mainly because the calculated $B(E2; 2_1{}^+ \rightarrow 0_1{}^+)$ value exceeds the experimental result. The $\langle Q^3 \cos(3\delta) \rangle$ invariant, however, indicates considerable triaxiality of the $0_1{}^+$ state, which is in agreement with the information deduced from the CWFs maps (Fig. 11).

The calculated $B(E2)$ values for the $0_2{}^+ \rightarrow 2_1{}^+$ and $0_2{}^+ \rightarrow 2_2{}^+$ transitions are also larger than the experimental findings. In addition, two 2^+ states at 3112 and 3441 keV decaying to the $0_2{}^+$ state are predicted, labeled in Figs. 10 and 11 as $2_3{}^+$ and $2_4{}^+$, respectively, with the computed $B(E2; 2_3{}^+ \rightarrow 0_2{}^+) = 22$ W.u. and $B(E2; 2_4{}^+ \rightarrow 0_2{}^+) = 11$ W.u. values. Therefore, the predicted overall collectivity is larger than the experimental one. The most plausible explanation for this effect is the use of an interaction, Gogny D1S in the present case, whose parameters were fitted to reproduce experimental data without taking into account the angular momentum projection. In general, the minima of angular momentum projected energy surfaces are obtained at larger deformations than the pure mean-field energy surfaces. Thus, the SCCM calculations inherit this flaw and tend to predict larger deformations than the experimental ones [78,79].

A $\rho^2(E0; 0_2{}^+ \rightarrow 0_1{}^+) \cdot 10^3 = 83$ has been calculated with the SCCM, which is more than one order of magnitude larger than the experimental value found in this work [4.0(15)]. This result reflects the large overlap between the CWFs of the $0^+_{1,2}$ states visible in Fig. 11 and suggests a considerable mixing between them, contrary to what was deduced from the experimental data.

Additionally, SCCM calculations including axial quadrupole and octupole degrees of freedom [80] were performed in order to investigate the octupole collectivity in ^{66}Zn. They yielded a value of $B(E3; 3_1{}^- \rightarrow 0_1{}^+) = 22$ W.u., which is in agreement with the previous result from electron scattering [20(3) W.u.] [57–59], but not with the value obtained in the present study ($2.8^{+0.8}_{-1.3}$ W.u.). Previous GCM calculations with Gogny functionals predicted a much lower value, consistent with the present experimental result (2.4 W.u. [81]). However, unlike the present SCCM

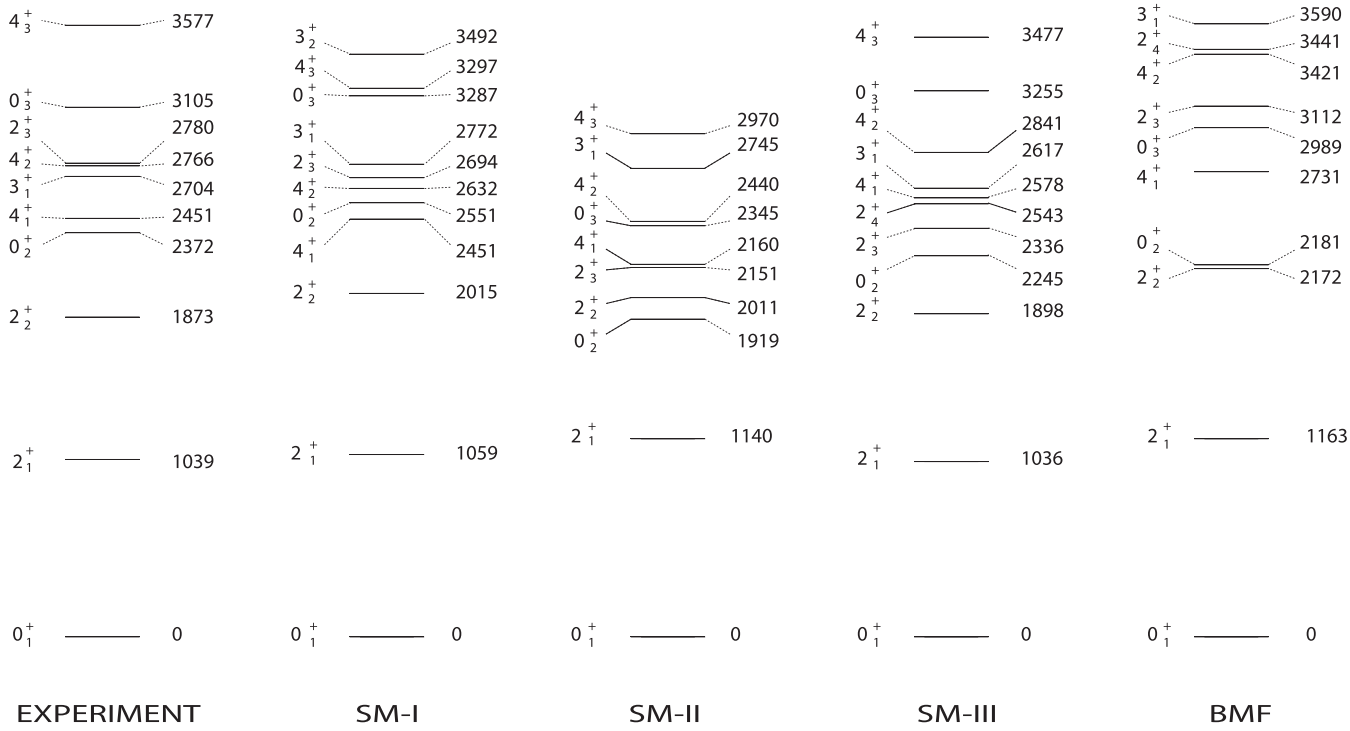

FIG. 10. Experimental level scheme of ^{66}Zn compared with those from BMF and SM calculations (see the text for details).

calculations, the previous ones did not take into account the angular momentum projection of the energies and the full interplay of quadrupole-octupole degrees of freedom. It was demonstrated that including the latter led to a significant increase of the $B(E3; 3_1^- \rightarrow 0_1^+)$ value in ^{64}Zn [82]. Nevertheless, since the ground state of ^{66}Zn is triaxially deformed, this puzzle will remain unsolved until full triaxial quadrupole-octupole calculations can eventually be performed.

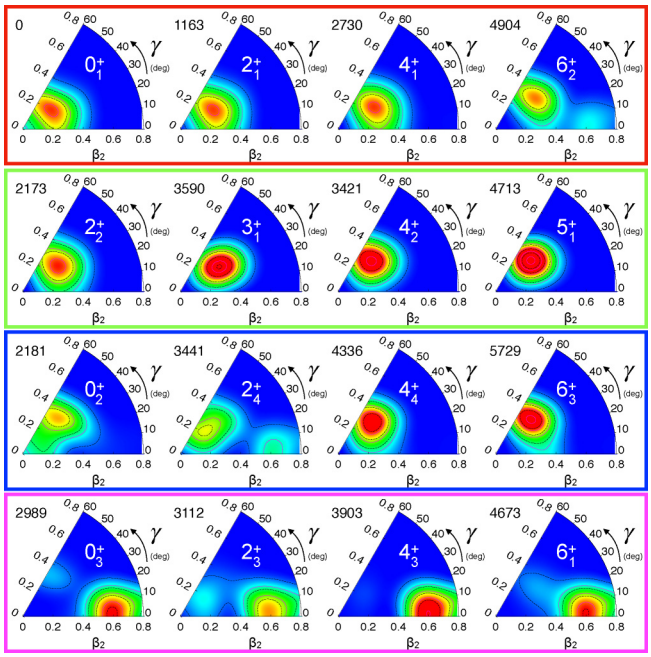

FIG. 11. Collective wave functions for selected states in ^{66}Zn, obtained within the SCCM framework. The energy of each state (in keV) is given on topleft of each CFW. The colored frames are used to present the suggested band assignments.

C. Large-scale shell-model calculations

Prior to the present study, several large-scale shell-model calculations were performed for ^{66}Zn using various cores and model spaces. In Refs. [37,38,83], the measured $B(E2)$ values in ^{66}Zn were compared with shell-model predictions using both ^{56}Ni and ^{40}Ca inert cores. The authors concluded that the role of the neutron $0g_{9/2}$ orbital is particularly important in the Zn isotopes and that further refinements in the effective nucleon-nucleon interaction were required to better describe their structure. However, the calculated $B(E2)$ values were

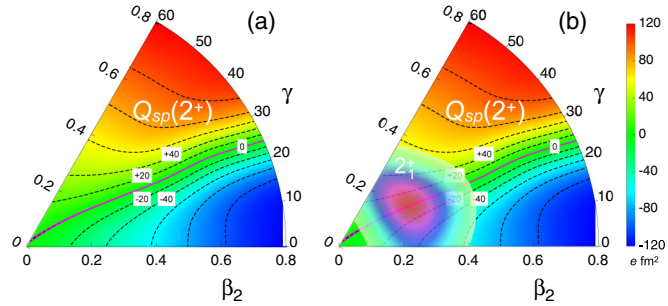

FIG. 12. (a) Spectroscopic quadrupole moment of the 2_1^+ state calculated as a function of (β_2, γ) parameters within the BMF framework. (b) Same as (a) but with the overlap of the CWF of the 2_1^+ state shown in Fig. 11.

reported only for the $2_1^+ \rightarrow 0_1^+$, $4_1^+ \rightarrow 2_1^+$ and $2_2^+ \rightarrow 0_1^+$ transitions. Since the present measurement yielded much more information about transition probabilities between the low-lying states in ^{66}Zn, new large-scale shell-model (SM) calculations were performed, using various effective interactions and considering different model spaces, in order to gain a better insight into the structure of this nucleus:

(1) In the SM calculations referred to as SM-I, the JUN45 effective interaction [84] was used, which is suitable for the model space $f_{5/2}pg_{9/2}$ for both protons and neutrons, considering ^{56}Ni as an inert core. The calculations adopted effective charges from Ref. [85] ($e_\pi = 1.8e$, $e_\nu = 0.8e$). The values $g_s^{(\text{eff.})} = 0.7 g_s^{(\text{free})}$ and $g_l^{(\text{eff.})} = g_l^{(\text{free})}$ were assumed as effective spin and orbital g factors, taken from Ref. [84].

(2) In SM-II, a modified version of the Lenzi-Nowacki-Poves-Sieja (LNPS) [86] effective interaction was used, referred to as LNPSU in the following, which has been extended towards $N = 50$ using a mapping from the PFSDG-U interaction in order to properly describe the particle-hole physics in the vicinity of ^{78}Ni [87,88]. The model space is based on a ^{48}Ca core and comprises the pf shell for protons and the $1p_{3/2}$, $1p_{1/2}$, $0f_{5/2}$, $0g_{9/2}$, and $1d_{5/2}$ orbitals for neutrons. The effective charges from Ref. [89] were adopted ($e_\pi = 1.31e$, $e_\nu = 0.46e$), whereas the assumed effective g factors follow the standard prescription of Ref. [90], i.e., $g_s^{(\text{eff.})} = 0.75 g_s^{(\text{free})}$ and $g_l^{(\text{eff.})} = -0.1$, $g_l^{(\text{eff.})} = 1.1$ for neutrons and protons, respectively.

(3) The SM-III calculations were performed considering a ^{56}Ni inert core and the model space $f_{5/2}pg_{9/2}$ for both protons and neutrons, as in the case of SM-I. The two-body matrix elements of the effective Hamiltonian were derived, within the framework of many-body perturbation theory, from the high-precision CD-Bonn NN potential [91] renormalized by means of the $V_{\text{low-k}}$ approach [92], with the addition of the Coulomb term for the proton-proton interaction. More precisely, the $\hat{Q}$ box folded-diagram approach was employed (Ref. [93] and references therein), including one- and two-body diagrams up to the third order in the interaction in the perturbative diagrammatic expansion of the $\hat{Q}$ box. The single-neutron and single-proton energies were taken, where possible, from the experimental energy spectra of ^{57}Ni [26] and ^{57}Cu [26], respectively, in order to take into account implicitly the effects of three-body forces on the single-particle energies. The energy of the proton $0g_{9/2}$, which is not available, was chosen to be the same as that of the neutron one, and it has been verified that a small variation of its value does not significantly affect the results for Zn isotopes. It is worth mentioning, however, that within SM-III the experimental excitation energy of the $9/2^+$ state at 604 keV in ^{67}Zn is underestimated by about 250 keV, which may be due to deficient monopole components of the two-body Hamiltonian (note that also JUN45, which includes monopole corrections and mass dependence of the TBME accounting for many-body correlations, underestimates the $9/2^+$ energy in ^{67}Zn, but only by ≈150 keV [84]). The effective $E2$ and $M1$ operators were calculated within the same framework of the shell-model Hamiltonian, by employing the Suzuki-Okamoto formalism [94]. Further details of this procedure, as well as the proton and neutron matrix elements of the effective $M1$ operator, can be found in Ref. [95]. The effective charges for the $E2$ operator are also state dependent and range from 1.8 to 1.3e for protons and from 1.4 to 0.8e for neutrons.

The SM-I and SM-II calculations were performed using the ANTOINE shell-model code [96,97], while for the SM-III calculations the KSHELL shell-model code [98] was used.

As shown in Fig. 10, the level energies calculated with SM-I are in good agreement with the experimental values, with typical differences below 100 keV. Only for the 0_2^+ state the calculations overestimate the experimental energy by about 200 keV. In this context, it is worth mentioning that a sudden increase of the 0_2^+ energy at $N = 36$ with respect to the neighboring isotopes has also been predicted by similar SM calculations for the Ge isotopes (JUN45 effective interaction and ^{56}Ni core [84]) and has been explained as a result of a delicate balance between the $N = 40$ single-particle energy gap and collective effects [84]. The principal component of the wave functions for the low-lying states resulting from SM-I is $\nu(0f_{5/2}^4 1p_{3/2}^4) \otimes \pi 1p_{3/2}^2$, except for the 2_2^+, 3_1^+, and 4_2^+ states for which the $1p_{1/2}$ neutron orbital becomes more important. The neutron $0g_{9/2}$ orbital is particularly relevant for the 0_2^+ state, with a calculated occupancy of 1.8 neutrons.

Similar to SM-I, the SM-II calculated level energies reproduce the experimental values well, except for those of the 0_2^+, 2_3^+, 4_1^+, and 4_2^+ states, which are underestimated by about 300 keV. The increased density of states stems from the extension of the model space with respect to SM-I and SM-III. In the calculations, the low-lying states have a dominant $\nu(0f_{5/2}^4 1p_{3/2}^4) \otimes \pi(0f_{7/2}^8 1p_{3/2}^2)$ configuration, with contributions of the $1p_{1/2}$ orbital in the 2_2^+ and 3_1^+ states, and $0f_{5/2}$ in the 4_2^+ state. The $0g_{9/2}$ neutron orbital significantly contributes to the 0_2^+ state: Similar to the SM-I calculations, an occupancy of 1.5 particles is predicted, in addition to an excitation from the $0f_{7/2}$ proton orbital to the $0f_{5/2}$. The neutron $1d_{5/2}$ orbital (which is the quadrupole partner of $0g_{9/2}$) appears to be not relevant for the structure of low-lying levels in ^{66}Zn, with a calculated occupancy of 0.02–0.1 particles.

The experimental excitation energy spectrum is reasonably well reproduced also by SM-III. All the calculated level energies differ by less than 120 keV from the corresponding experimental values. The only exception is the 2_3^+ state, whose energy is underestimated by about 500 keV. However, as shown in Fig. 10, a fourth 2^+ state is predicted, with an energy close to that of the experimental 2_3^+ state. In contrast to SM-I and SM-II, the main component of all the low-lying states is $\nu(0f_{5/2}^2 1p_{3/2}^4 1p_{1/2}^2) \otimes \pi 1p_{3/2}^2$, except for the 4_2^+ and 3_1^+ states, which, instead, are dominated by the $\nu(0f_{5/2}^3 1p_{3/2}^4 1p_{1/2}^1) \otimes \pi 1p_{3/2}^2$ configuration. The occupancy of the $0g_{9/2}$ neutron orbital is 0.3–0.8 for all the states. In contrast with SM-I and SM-II, this is valid also for the 0_2^+

state, for which the occupation of the $0g_{9/2}$ neutron orbital is 0.8.

The comparison of the experimental $B(\frac{E}{M}\lambda)$ and Q_s values obtained in this work with those resulting from the calculations is presented in Table II. The known $B(E2; 2_1^+ \rightarrow 0_1^+)$ value is well reproduced by the theoretical predictions with the exception of SM-II that slightly underestimates this transition probability. None of the SM calculations reproduce the two features of ^{66}Zn typically related to enhanced triaxiality, namely the enhancement of the $B(E2; 2_2^+ \rightarrow 2_1^+)$ value with respect to $B(E2; 2_1^+ \rightarrow 0_1^+)$, or the strong hindrance of the $B(E2; 2_2^+ \rightarrow 0_1^+)$ value. Much smaller transition probabilities for the $0_2^+ \rightarrow 2_2^+$ and $0_2^+ \rightarrow 2_1^+$ transitions are obtained within the SM calculations than with the BMF approach, in reasonable agreement with the experimental values. The $B_{4/2}$ ratio is predicted to be less than 1 by all SM calculations; however, the calculated $B(E2; 4_2^+ \rightarrow 2_1^+)$ values are larger than the calculated $B(E2; 4_1^+ \rightarrow 2_1^+)$ values, suggesting that the 4_1^+ and 4_2^+ states may be inverted in the calculations with respect to the experimental data. This suggestion is further supported by the comparison of the experimental and calculated spectroscopic quadrupole moments. In fact, the experimental results and BMF calculations show that $Q_s(4_1^+)$ and $Q_s(2_1^+)$ have the same signs, while in all SM calculations it is the second 4^+ state that has the same Q_s sign as the 2_1^+ state (note that SM-III predicts the same sign for both the $4_{1,2}^+$ states). This inversion could be due to inaccuracies of the monopole component of the SM Hamiltonian in describing the evolution of the single-particle levels, in particular that of the $0g_{9/2}$ orbital.

Similar to the BMF approach, all the SM calculations predict a negative sign of the $Q_s(2_1^+)$, in contrast to the present experimental result. Furthermore, the signs of the experimental Q_s values of the first two 2^+ states are reversed with respect to all the theoretical predictions. A similar inversion is observed for the Q_s of the 4_2^+ state (tentatively identified as the experimental 4_1^+ state). Contrary to the BMF calculations, the magnitude of the $Q_s(2_1^+)$ is reproduced well by the SM calculations, with a slight underestimation observed for SM-II. Since the calculated $Q_s(2_2^+)$ has an opposite sign with respect to $Q_s(2_1^+)$, in addition to the fact that $Q_s(3_1^+)$ is predicted to be close to zero and the $B(E2; 3_1^+ \rightarrow 2_2^+)$ to be large (see Table II), the 2_2^+ state in the SM calculations can be interpreted as the bandhead of a γ band, in agreement with the conclusions from the analysis of the CWFs in the BMF calculations.

The excitation energies, transition probabilities and quadrupole moments that were obtained with SM-I and SM-III, which assume the same inert core and model space, are rather similar. Even though the wave functions resulting from the two calculations show different configuration mixing, these results indicate that consistent renormalizations are induced in the Hamiltonian and the bare one-body operators by the perturbative approach within SM-III.

Typically, $E3$ transitions that are measurable in Coulomb-excitation experiments are related to collective excitations and, consequently, reproducing them lies beyond the range of shell-model spaces that are available. Hence, both excitation energies of negative-parity states and transition probabilities

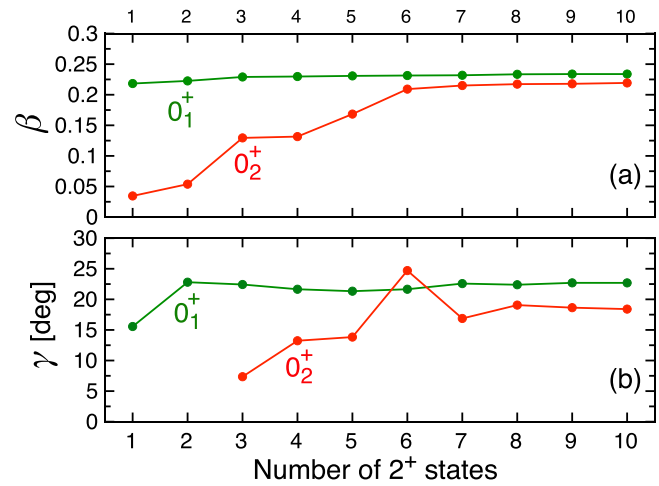

FIG. 13. Deformation parameters β (a) and γ (b) of the 0_1^+ and 0_2^+ states (green and red, respectively) calculated with SM-III as a function of the number of considered 2^+ states. For the γ parameter of the 0_2^+ state, the calculations give unphysical $\cos(3\delta) > 1$ values if only one or two 2^+ states are considered.

involving those were not expected to be well reproduced by any of the SM calculations presented here. While they indeed predict the 3_1^- state to be about 1 MeV higher in energy than observed, it is interesting to note that the $B(E3; 3_1^- \rightarrow 0_1^+) = 5.0$ W.u. calculated with SM-I is in reasonable agreement with the experimental value obtained in the present work.

The quadrupole sum rules method was applied to the theoretical sets of matrix elements, as reported in Tables IV and V. For all the SM calculations, the deduced $\langle Q^2 \rangle$ and $\langle Q^3 \cos(3\delta) \rangle$ invariants for the ground state are strongly dominated by the $\langle 0_1^+||E2||2_1^+\rangle\langle 2_1^+||E2||0_1^+\rangle$ and $\langle 0_1^+||E2||2_1^+\rangle\langle 2_1^+||E2||2_1^+\rangle\langle 2_1^+||E2||0_1^+\rangle$ products, respectively, as it was observed for the invariants resulting from the BMF calculations and the experimental results. An enhanced nonaxiality in the ground state of ^{66}Zn is also predicted within the SM calculations, providing a possible explanation for the observed disagreement in the sign of the spectroscopic quadrupole moments, as has been discussed for the BMF calculations. However, a more prolate centroid is predicted with respect to the experimental result by SM-I and SM-III, i.e., considering the ^{56}Ni core. Regarding the 0_2^+ state, a much smaller deformation is predicted by the SM calculations with respect to the BMF approach when only the first two 2^+ states are considered. However, an analysis performed with SM-III showed that when more 2^+ states are taken into account in the quadrupole sum rules analysis, the deformation of this state becomes closer to that of the ground state (see Fig. 13). This could indicate a scenario similar to what was recently found for ^{72}Ge, where shape coexistence between triaxial and spherical structures was initially suggested [99]. Later, however, the observation of additional 2^+ states decaying to the 0_2^+ state led to the conclusion that while two coexisting structures are indeed present in the ^{72}Ge nucleus, they are both characterized by deformed nonaxial shapes [100]. It should be noted that while the present calculations show that matrix elements involving several higher

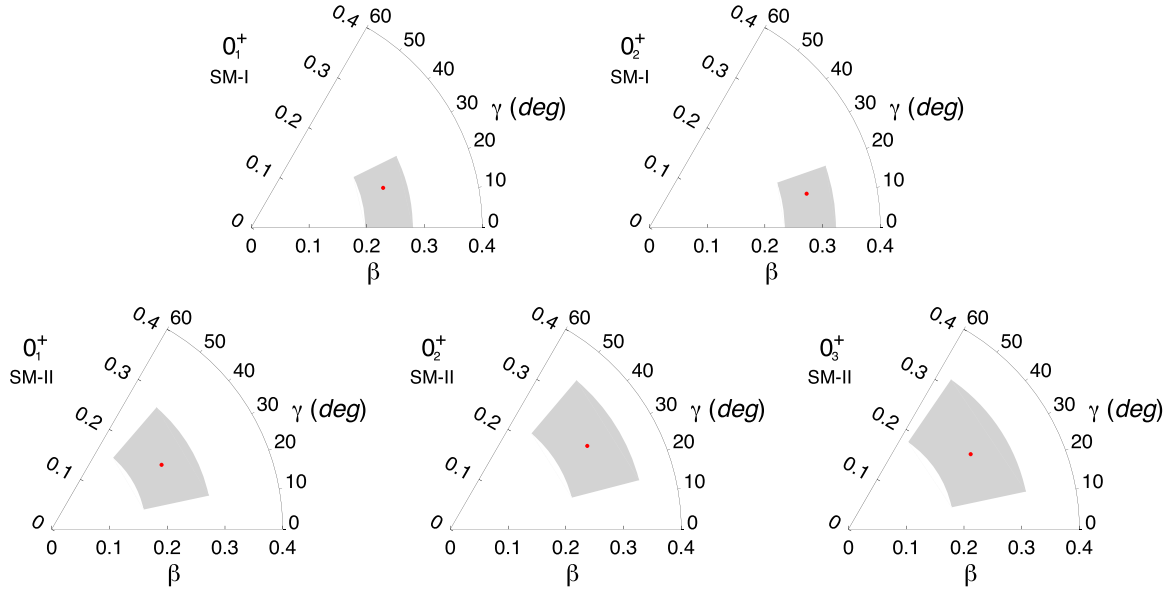

FIG. 14. The β and γ deformation parameters (red dots) calculated for 0^+ states in ^{66}Zn with JUN45 (top) and LNPSU (bottom) interactions. The gray areas illustrate the variance of these parameters.

lying 2^+ states are necessary to obtain deformation parameters for the $0_2{}^+$ state in ^{66}Zn, this cannot be generalized to all nuclei, as, for example, in Refs. [66,68] it was demonstrated that the $E2$ strength related to the $0_2{}^+$ states in ^{100}Mo and ^{42}Ca, respectively, was practically exhausted by transitions to the first three 2^+ states.

Finally, the β and γ deformation parameters were calculated within the framework of the configuration-interaction shell-model [71]. This novel method was developed to accurately calculate higher order quadrupole invariants related to the fluctuations of the intrinsic deformation parameters. The advantage of this approach is that the expectation values of these invariants can be calculated using the projected Lanczos strength function method, naturally incorporated in the shell-model codes. The values of the deformation parameters and their fluctuations calculated using the ANTOINE shell-model code [96,97] for SM-I and SM-II are presented in Fig. 14. The calculations with both the JUN45 and LNPSU effective interactions predict large fluctuations of the deformation parameters, with the latter systematically resulting in more nonaxial shapes for the first three 0^+ states. With both interactions, a similar deformation of the $0_2{}^+$ state with respect to the ground state is predicted, in agreement with the results obtained with SM-III (see Fig. 13).

V. SUMMARY

Electromagnetic properties of low-lying states in ^{66}Zn were investigated using the Coulomb-excitation method at the INFN Legnaro National Laboratories. The experiment used, for the first time, the newly installed and commissioned SPIDER charged-particle array, in combination with the GALILEO γ-ray spectrometer. A set of reduced $E2$, $E3$, and $M1$ matrix elements was extracted from the collected data using the GOSIA code, allowing for the determination of 12 reduced transition probabilities and the spectroscopic quadrupole moment of the first excited 2^+ state. In addition, the upper and lower limits for the $B(E2; 2_3{}^+ \rightarrow 4_1{}^+)$ value as well as the signs of the $Q_s(4_1{}^+)$, $Q_s(2_2{}^+)$ spectroscopic quadrupole moments were determined.

The obtained spectroscopic data are in general agreement with previous measurements as well as with the systematic trends in the Zn isotopic chain. Furthermore, when more than one value was available in the literature, the achieved experimental precision allowed us to discriminate between the discrepant results.

The previously unknown reduced transition probabilities for the transitions de-exciting the $0_2{}^+$ state have been extracted. Consequently, the deduced lifetime of this state led to the first determination of the $\rho^2(E0; 0_2{}^+ \rightarrow 0_1{}^+)$ value. Furthermore, the $B(E3; 3_1{}^- \rightarrow 0_1{}^+)$ value has been determined for the first time in a Coulomb-excitation measurement, suggesting that octupole collectivity in ^{66}Zn may not be as enhanced as previously thought. Thanks to the sensitivity of the present experiment to the relative signs of several key $E2$ matrix elements, it was possible to apply the quadrupole sum rules method in order to study the shape of the ground state and the $0_2{}^+$ state. Following these results, the obtained deformation parameters combined with the $\rho^2(E0; 0_2{}^+ \rightarrow 0_1{}^+)$ value provided a measure of the mixing between the two 0^+ states within the two-level mixing model.

The obtained experimental results indicate a complex structure of the low-lying states of ^{66}Zn, which cannot be consistently interpreted within the framework of simple collective models. Consequently, extensive beyond-mean-field and large-scale shell-model calculations with a variety of model spaces and interactions were performed. All the calculations reproduce reasonably well the excitation energies of the low-lying states in ^{66}Zn. The BMF calculations globally reproduce its electromagnetic properties, even though the

quadrupole and octupole collectivity appear to be overestimated. The main conclusion from the comparison of different SM calculations, carried out using various model spaces with different interactions and effective charges, is that the $f_{5/2}pg_{9/2}$ model space seems to be sufficient to describe the structure of ^{66}Zn at low excitation energy, even though the $d_{5/2}$ and $f_{7/2}$ orbitals are expected to be required to properly describe heavier Zn isotopes and the development of larger quadrupole collectivity. The overall reproduction of experimental data by SM calculations is satisfactory, with important similarities observed between the SM-I and SM-III results, which use the same model space. In particular, all three calculations predict a similar deformation of the 0_2^+ state with respect to the ground state. They fail, however, to reproduce some of the ^{66}Zn properties, such as the ordering of the first two 4^+ states and the $E2$ transition rates from the second 2^+ state, which points out to specific shortcomings in the employed effective interactions.

The importance of the triaxial degree of freedom emerges from the experimental and theoretical results (BMF and LNPS calculations in particular), with the latter indicating that most of the low-lying states in ^{66}Zn exhibit rather diffuse shapes. This provides a possible explanation of the disagreement between the experimental sign of $Q_s(2_1^+)$ and the theoretical predictions, relating it to large fluctuations of wave functions around $\gamma \approx 30^\circ$. This analysis demonstrates once again that, for nuclei exhibiting significant nonaxiality, going beyond a simple comparison of spectroscopic quadrupole moments by means of the quadrupole sum rules method is more conclusive, in agreement with the recent results on ^{76}Se [101].

The present results indicate a spherical character of the 0_2^+ state and its weak connection to other low-lying states. However, beyond-mean-field and shell-model calculations predict for this state a deformation similar to that of the ground state, related to non-negligible $E2$ transitions to higher lying 2^+ states. In this context, further experimental studies aiming at identification of 2^+ states that would decay to the first excited 0^+ state are necessary to firmly establish the coexisting shapes in ^{66}Zn.

ACKNOWLEDGMENTS

The authors would like to thank the staff of the LNL Tandem-XTU accelerator for the high quality of the delivered ^{66}Zn beam, M. Loriggiola for producing the targets, and the mechanical workshops of the INFN divisions of Florence, LNL, and Padua for their crucial contribution. We also would like to thank L. P. Gaffney, P. E. Garrett, L. M. Robledo, J. Srebrny, and K. Wrzosek-Lipska for the fruitful discussions. This work was supported by the National Science Centre, Poland, under Projects No. DEC- 2014/12/S/ST2/00483 and No. 2014/14/M/ST2/00738 (COPIN-INFN Collaboration) and by the Spanish Ministerio de Ciencia en Innovación under Grant No. PGC2018-094583-B-I00. G.D.G. and A.G. acknowledge the CINECA award under the ISCRA initiative and through the INFN-CINECA agreement for the availability of high-performance computing resources and support. G.D.G. acknowledges also the support by the funding program "VALERE" of Università degli Studi della Campania "Luigi Vanvitelli."

[1] S. Leoni, B. Fornal, N. Mărginean, M. Sferrazza, Y. Tsunoda, T. Otsuka, G. Bocchi, F. C. L. Crespi, A. Bracco, S. Aydin *et al.*, Phys. Rev. Lett. **118**, 162502 (2017).

[2] J. Ljungvall, A. Görgen, M. Girod, J. P. Delaroche, A. Dewald, C. Dossat, E. Farnea, W. Korten, B. Melon, R. Menegazzo, A. Obertelli, R. Orlandi, P. Petkov, T. Pissulla, S. Siem, R. P. Singh, J. Srebrny, Ch. Theisen, C. A. Ur, J. J. Valiente-Dobón, K. O. Zell, and M. Zielińska, Phys. Rev. Lett. **100**, 102502 (2008).

[3] Y. Toh, T. Czosnyka, M. Oshima, T. Hayakawa, H. Kusakari, M. Sugawara, A. Osa, M. Koizumi, Y. Hatsukawa, J. Katakura, N. Shinohara, and M. Matsuda, J. Phys. G: Nucl. Part. Phys. **27**, 1475 (2001).

[4] J. L. Wood, K. Heyde, W. Nazarewicz, M. Huyse, and P. V. Duppen, Phys. Rep. **215**, 101 (1992).

[5] A. Passoja, R. Julin, J. Kantele, and M. Luontama, Nucl. Phys. A **363**, 399 (1981).

[6] M. Koizumi, A. Seki, Y. Toh, A. Osa, Y. Utsuno, A. Kimura, M. Oshima, T. Hayakawa, Y. Hatsukawa, J. Katakura, M. Matsuda, T. Shizuma, T. Czosnyka, M. Sugawara, T. Morikawa, and H. Kusakari, Nucl. Phys. A **730**, 46 (2004).

[7] Nihad J. Abu Awwad, H. Abusara, and S. Ahmad, Phys. Rev. C **101**, 064322 (2020).

[8] C. Y. Song, Z. P. Li, D. Vretenar, and J. Meng, Sci. China: Phys., Mech. Astron. **54**, 222 (2011).

[9] D. N. Simister, G. D. Jones, A. Kogan, P. R. G. Lornie, T. P. Morrison, M. Mustaffa, H. G. Price, P. J. Twin, and R. Wadsworth, J. Phys. G: Nucl. Part. Phys. **4**, 111 (1978).

[10] A. Passoja, R. Julin, J. Kantele, J. Kumpulainen, M. Luontama, and W. Trzaska, Nucl. Phys. A **438**, 413 (1985).

[11] P. E. Garrett, T. R. Rodríguez, A. Diaz Varela, K. L. Green, J. Bangay, A. Finlay, R. A. E. Austin, G. C. Ball, D. S. Bandyopadhyay, V. Bildstein *et al.*, Phys. Rev. Lett. **123**, 142502 (2019).

[12] P. E. Garrett and J. L. Wood, J. Phys. G: Nucl. Part. Phys. **37**, 064028 (2010).

[13] D. N. Simister, G. D. Jones, F. Kearns, A. Kogan, P. R. G. Lornie, T. P. Morrison, M. Mustaffa, H. G. Price, P. J. Twin, and R. Wadsworth, J. Phys. G: Nucl. Part. Phys. **4**, 1127 (1978).

[14] M. Koizumi, A. Seki, Y. Toh, M. Oshima, A. Osa, A. Kimura, Y. Hatsukawa, T. Shizuma, T. Hayakawa, M. Matsuda, J. Katakura, T. Czosnyka, M. Sugawara, T. Morikawa, and H. Kusakari, Eur. Phys. J. A **18**, 87 (2003).

[15] A. Gade, H. Klein, N. Pietralla, and P. von Brentano, Phys. Rev. C **65**, 054311 (2002).

[16] K. Kumar, Phys. Rev. Lett. **28**, 249 (1972).

[17] M. Rocchini, K. Hadyńska-Klęk, A. Nannini, J. J. Valiente-Dobón, A. Goasduff, D. Testov, P. R. John, D. Mengoni, M. Zielinska, D. Bazzacco *et al.*, Phys. Scr. **92**, 074001 (2017).

[18] D. Cline, Annu. Rev. Nucl. Part. Sci. **36**, 683 (1986).

[19] K. Alder and A. Winther, *Electromagnetic Excitation* (North-Holland, Amsterdam, 1975).

[20] J. J. Valiente-Dobón, D. Mengoni, F. Recchia, G. de Angelis, D. Barrientos, D. Bazzacco, M. Bellato, A. Benato, M. Bettini, L. Berti *et al.*, INFN LNL Annual Report **2014**, 95 (2015).

[21] D. Testov, D. Mengoni, A. Goasduff, A. Gadea, R. Isocrate, P. R. John, G. de Angelis, D. Bazzacco, C. Boiano, A. Boso *et al.*, Eur. Phys. J. A **55**, 47 (2019).

[22] M. Rocchini, K. Hadyńska-Klęk, A. Nannini, J. J. Valiente-Dobón, A. Goasduff, D. Testov, D. Mengoni, P. R. John, M. Siciliano, B. Melon *et al.*, Nucl. Instrum. Methods Phys. Res. A **971**, 164030 (2020).

[23] M. Rocchini, M. Chiari, E. Pasquali, A. Nannini, K. Hadyńska-Klęk, P. Sona, D. Bazzacco, G. Benzoni, F. Camera, C. Czelusniak *et al.*, Nucl. Instrum. Methods Phys. Res. B **486**, 68 (2021).

[24] P. A. Mandó, Nucl. Phys. News **19**, 5 (2009).

[25] T. Czosnyka, D. Cline, and C. Y. Wu, Bull. Am. Phys. Soc. **28**, 745 (1982).

[26] Data extracted using the NNDC On-Line Data Service from the ENSDF database [http://www.nndc.bnl.gov/ensdf/], files revised as of April 2012 (^{62}Zn), December 2006 (^{64}Zn), March 2009 (^{66}Zn), March 2012 (^{68}Zn), July 2016 (^{70}Zn), and September 1998 (^{57}Cu, ^{57}Ni).

[27] N. Shikazono and Y. Kawarsaki, Nucl. Phys. A **118**, 114 (1968).

[28] C. M. Baglin, E. Browne, E. B. Norman, G. L. Molnar, T. Belgya, Z. Revay, and F. Szelecsenyi, Nucl. Instrum. Methods Phys. Res. A **481**, 365 (2002).

[29] M. M. Be, V. Chiste, C. Dulieu, E. Browne, V. Chechev, N. Kuzmenko, R. Helmer, A. Nichols, E. Schonfeld, and R. Dersch, Table of Radionuclides (Vol. 1 - A = 1 to 150), BIPM-5 (2004).

[30] B. Erlandsson, J. Lyttkens, K. Nilson, and A. Marcinkowski, Phys. Scr. **22**, 432 (1980).

[31] J. K. Smith, A. D. MacLean, W. Ashfield, A. Chester, A. B. Garnsworthy, and C. E. Svensson, Nucl. Instrum. Methods Phys. Res. A **922**, 47 (2019).

[32] T. R. Fisher and P. D. Bond, Part. Nucl. **6**, 119 (1973).

[33] D. K. Kaipov, Y. G. Kosyak, L. N. Smirin, and Y. K. Shubnyi, Izv. Akad. Nauk SSSR, Ser. Fiz. **36**, 137 (1972); Bull. Acad. Sci. USSR, Phys. Ser. **36**, 128 (1973).

[34] Y. Cauchois, H. Ben Abdelaziz, R. Kherouf, and C. Schloesing-Moller, J. Phys. G: Nucl. Phys. **7**, 1539 (1981).

[35] R. G. Arnold, Ph.D. thesis, University of Boston, Boston, MA, 1972); Diss. Abst. Int. **33B**, 1723 (1972).

[36] R. B. Begzhanov and A. A. Islamov, Yadern. Fiz. **5**, 483 (1967); Sov. J. Nucl. Phys. **5**, 339 (1967).

[37] J. Leske, K. H. Speidel, S. Schielke, J. Gerber, P. Maier-Komor, T. Engeland, and M. Hjorth-Jensen, Phys. Rev. C **73**, 064305 (2006).

[38] O. Kenn, K. H. Speidel, R. Ernst, S. Schielke, S. Wagner, J. Gerber, P. Maier-Komor, and F. Nowacki, Phys. Rev. C **65**, 034308 (2002).

[39] R. Neuhausen, Nucl. Phys. A **282**, 125 (1977).

[40] M. Ivascu, D. Popescu, E. Dragulescu, V. Avrigeanu, C. Besliu, and N. Martalogu, Nucl. Phys. A **218**, 104 (1974).

[41] D. H. Youngblood, R. L. Kozub, and J. C. Hill, Nucl. Phys. A **183**, 197 (1972).

[42] U. Y. Zhovliev, M. F. Kudoyarov, I. Kh. Lemberg, and A. A. Pasternak, Izv. Akad. Nauk SSSR, Ser. Fiz. **45**, 1879 (1981).

[43] G. F. Neal, Z. P. Sawa, F. P. Venezia, and P. R. Chagnon, Nucl. Phys. A **280**, 161 (1977).

[44] J. F. Bruandet, M. Agard, A. Giorni, J. P. Longequeue, C. Morand, and T. U. Chan, Phys. Rev. C **12**, 1739 (1975).

[45] L. Cleemann, J. Eberth, W. Neuman, and V. Zobel, Nucl. Phys. A **386**, 367 (1982).

[46] K. Kaipov, Y. G. Kosyak, A. I. Serebrennikov, L. V. Chekushina, and A. M. Demidov, in *Proc. 30th Ann. Conf. Nucl. Spectrosc. Struct. At. Nuclei* (Nauka, Moscow-Leningrad, 1980), p. 52.

[47] L. N. Smirin, D. K. Kaipov, A. I. Serebrennikov, A. N. Demidov, and L. I. Govor, in *Proc. 26th Ann. Conf. Nucl. Spectrosc. Struct. At. Nuclei* (Nauka, Moscow-Leningrad, 1976), p. 58.

[48] J. K. Dickens, Nucl. Sci. Eng. **58**, 331 (1975).

[49] Y. G. Kosyak, D. K. Kanipov, L. V. Chekushina, and G. A. Dostemesova, Izv. Akad. Nauk SSSR, Ser. Fiz. **49**, 895 (1985); Y. G. Kosyak, D. K. Kanipov, L. V. Chekushina, G. A. Dostemesova, Bull. Acad. Sci. USSR, Phys. Ser. **49**, 55 (1985).

[50] F. R. Metzger, Nucl. Phys. A **189**, 409 (1972).

[51] M. Zielińska, L. P. Gaffney, K. Wrzosek-Lipska, E. Clément, T. Grahn, N. Kesteloot, P. Napiorkowski, J. Pakarinen, P. Van Duppen, and N. Warr, Eur. Phys. J. A **52**, 99 (2016).

[52] T. Kibedi, T. W. Burrows, M. B. Trzhaskovskaya, P. M. Davidson, and C. W. Nestor, Jr., Nucl. Instrum. Methods Phys. Res. A **589**, 202 (2008).

[53] J. F. Ziegler, Nucl. Instrum. Methods Phys. Res. B **219–220**, 1027 (2004).

[54] J. Srebrny, T. Czosnyka, W. Karczmarczyk, P. Napiorkowski, Ch. Droste, H.-J. Wollersheim, H. Emling, H. Grein, R. Kulessa, D. Cline, and C. Fahlander, Nucl. Phys. A **557**, 663c (1993).

[55] L. A. Currie, Anal. Chem. **40**, 587 (1968).

[56] M. Zielińska and K. Hadyńska-Klęk, EPJ Web Conf. **178**, 02014 (2018).

[57] T. Kibedi and R. H. Spear, At. Data Nucl. Data Tables **80**, 35 (2002).

[58] R. Neuhausen, J. W. Lightbody Jr., S. P. Fivozinsky, and S. Penner, Nucl. Phys. A **263**, 249 (1976).

[59] V. D. Afanasev, N. G. Afanasev, A. Y. Buki, G. A. Savitskii, V. M. Khvastunov, and N. G. Shevchenko, Yad. Fiz. **12**, 885 (1970); Sov. J. Nucl. Phys. **12**, 480 (1971).

[60] W. K. Koo and L. J. Tassie, J. Phys. G: Nucl. Part. Phys. **7**, L63 (1981).

[61] S. Agostinelli, J. Allison, K. Amako, J. Apostolakis, H. Araujo, P. Arce, M. Asai, D. Axen, S. Banerjee, G. Barrand *et al.*, Nucl. Instrum. Methods Phys. Res. A **506**, 250 (2003).

[62] S. Salem-Vasconcelos, M. J. Bechara, J. H. Hirata, and O. Dietzsch, Phys. Rev. C **38**, 2439 (1988).

[63] C. Mihai, N. V. Zamfir, D. Bucurescu, G. Cata-Danil, I. Cata-Danil, D. G. Ghita, M. Ivascu, T. Sava, L. Stroe, and G. Suliman, Phys. Rev. C **75**, 044302 (2007).

[64] C. Louchart, A. Obertelli, A. Görgen, W. Korten, D. Bazzacco, B. Birkenbach, B. Bruyneel, E. Clement, P. J. Coleman-Smith, L. Corradi *et al.*, Phys. Rev. C **87**, 054302 (2013).

[65] J. Srebrny and D. Cline, Int. J. Mod. Phys. E **20**, 422 (2011).

[66] K. Wrzosek-Lipska, L. Próchniak, M. Zielińska, J. Srebrny, K. Hadynska-Klek, J. Iwanicki, M. Kisielinski, M. Kowalczyk, P. J. Napiorkowski, D. Pietak, and T. Czosnyka, Phys. Rev. C **86**, 064305 (2012).

[67] N. Bree, K. Wrzosek-Lipska, A. Petts, A. Andreyev, B. Bastin, M. Bender, A. Blazhev, B. Bruyneel, P. A. Butler, J. Butterworth *et al.*, Phys. Rev. Lett. **112**, 162701 (2014).
[68] K. Hadyńska-Klęk, P. Napiorkowski, M. Zielińska, J. Srebrny, A. Maj, F. Azaiez, J. J. Valiente Dobón, M. Kicinska-Habior, F. Nowacki, H. Naïdja *et al.*, Phys. Rev. C **97**, 024326 (2018).
[69] W. Andrejtscheff and P. Petkov, Phys. Lett. B **329**, 1 (1994).
[70] E. Clément, A. Görgen, W. Korten, E. Bouchez, A. Chatillon, J.-P. Delaroche, M. Girod, H. Goutte, A. Hurstel, Y. Le Coz, *et al.*, Phys. Rev. C **75**, 054313 (2007).
[71] A. Poves, F. Nowacki, and Y. Alhassid, Phys. Rev. C **101**, 054307 (2020).
[72] T. R. Rodríguez and J. L. Egido, Phys. Rev. C **81**, 064323 (2010).
[73] J. F. Berger, M. Girod, and D. Gogny, Nucl. Phys. A **428**, 23 (1984).
[74] M. Anguiano, J. L. Egido, and L. M. Robledo, Nucl. Phys. A **696**, 467 (2001).
[75] P. Ring and P. Schuck, *The Nuclear Many Body Problem* (Springer-Verlag, Berlin, 1980).
[76] J. L. Egido, M. Borrajo, and T. R. Rodríguez, Phys. Rev. Lett. **116**, 052502 (2016).
[77] T. R. Rodríguez, Eur. Phys. J. A **52**, 190 (2016).
[78] M. Bender, G. F. Bertsch, and P.-H. Heenen, Phys. Rev. C **73**, 034322 (2006).
[79] T. R. Rodríguez, A. Arzhanov, and G. Martínez-Pinedo, Phys. Rev. C **91**, 044315 (2015).
[80] R. N. Bernard, L. M. Robledo, and T. R. Rodríguez, Phys. Rev. C **93**, 061302(R) (2016).
[81] L. M. Robledo, Eur. Phys. J. A **52**, 300 (2016).
[82] L. M. Robledo, EPJ Web Conf. **66**, 02091 (2014).
[83] K. Moschner, K. H. Speidel, J. Leske, C. Bauer, C. Bernards, L. Bettermann, M. Honma, T. Moller, P. Maier-Komor, and D. Mücher, Phys. Rev. C **82**, 014301 (2010).
[84] M. Honma, T. Otsuka, T. Mizusaki, and M. Hjorth-Jensen, Phys. Rev. C **80**, 064323 (2009).
[85] S. Mukhopadhyay, B. P. Crider, B. A. Brown, S. F. Ashley, A. Chakraborty, A. Kumar, M. T. McEllistrem, E. E. Peters, F. M. Prados-Estévez, and S. W. Yates, Phys. Rev. C **95**, 014327 (2017).
[86] S. M. Lenzi, F. Nowacki, A. Poves, and K. Sieja, Phys. Rev. C **82**, 054301 (2010).
[87] F. Nowacki, A. Poves, E. Caurier, and B. Bounthong, Phys. Rev. Lett. **117**, 272501 (2016).
[88] R. Taniuchi, C. Santamaria, P. Doornenbal, A. Obertelli, K. Yoneda, G. Authelet, H. Baba, D. Calvet, F. Chateau, A. Corsi *et al.*, Nature (London) **569**, 52 (2019).
[89] M. Dufour and A. P. Zuker, Phys. Rev. C **54**, 1641 (1996).
[90] E. Caurier, A. Poves, and A. P. Zuker, Phys. Lett. **256**, 301 (1991).
[91] R. Machleidt, Phys. Rev. C **63**, 024001 (2001).
[92] S. Bogner, T. T. S. Kuo, and L. Coraggio, Nucl. Phys. A **684**, 432c (2001).
[93] L. Coraggio, A. Covello, A. Gargano, N. Itaco, and T. T. S. Kuo, Ann. Phys. **327**, 2125 (2012).
[94] K. Suzuki and R. Okamoto, Prog. Theor. Phys. **93**, 905 (1995).
[95] L. Coraggio, L. De Angelis, T. Fukui, A. Gargano, N. Itaco, and F. Nowacki, Phys. Rev. C **100**, 014316 (2019).
[96] E. Caurier and F. Nowacki, Acta. Phys. Pol. B **30**, 749 (1999).
[97] E. Caurier, G. Martinez-Pinedo, F. Nowacki, A. Poves, and A. P. Zuker, Rev. Mod. Phys. **77**, 427 (2005).
[98] N. Shimizu, T. Mizusaki, T. Utsuno, and Y. Tsunoda, Comput. Phys. Commun. **244**, 372 (2019).
[99] B. Kotlinski, T. Czosnyka, D. Cline, J. Srebrny, C. Y. Wu, A. Backlin, L. Hasselgren, L. Westerberg, C. Baktash, and S. G. Steadman, Nucl. Phys. A **519**, 646 (1990).
[100] A. D. Ayangeakaa, R. V. F. Janssens, C. Y. Wu, J. M. Allmond, J. L. Wood, S. Zhu, M. Albers, S. Almaraz-Calderon, B. Bucher, M. P. Carpenter *et al.*, Phys. Lett. B **754**, 254 (2016).
[101] J. Henderson, C. Y. Wu, J. Ash, B. A. Brown, P. C. Bender, R. Elder, B. Elman, A. Gade, M. Grinder, H. Iwasaki *et al.*, Phys. Rev. C **99**, 054313 (2019).